

## RESEARCH ARTICLE

10.1002/2014JE004654

## Key Points:

- Modeling seismicity in highly scattering media
- Studying the effects of the interior structure on scattered codas
- Coda is most affected by the presence of shallow low-velocity layers

## Correspondence to:

J.-F. Blanchette-Guertin,  
blanchetteg@ipgp.fr

## Citation:

Blanchette-Guertin, J.-F., C. L. Johnson, and J. F. Lawrence (2015), Modeling seismic energy propagation in highly scattering environments, *J. Geophys. Res. Planets*, 720, doi:10.1002/2014JE004654.

Received 16 APR 2014

Accepted 6 FEB 2015

Accepted article online 11 FEB 2015

## Modeling seismic energy propagation in highly scattering environments

J.-F. Blanchette-Guertin<sup>1,2</sup>, C. L. Johnson<sup>2,3</sup>, and J. F. Lawrence<sup>4</sup>

<sup>1</sup>Equipe Planétologie et Sciences Spatiales, Université Paris Diderot, Sorbonne Paris Cité, Institut de Physique du Globe de Paris, UMR 7154, CNRS, Paris, France, <sup>2</sup>Department of Earth, Ocean and Atmospheric Sciences, University of British Columbia, Vancouver, British Columbia, Canada, <sup>3</sup>Planetary Science Institute, Tucson, Arizona, USA, <sup>4</sup>Department of Geophysics, Stanford University, Stanford, California, USA

**Abstract** Meteoroid impacts over millions to billions of years can produce a highly fractured and heterogeneous megaregolith layer on planetary bodies such as the Moon that lack effective surface recycling mechanisms. The energy from seismic events on these bodies undergoes scattering in the fractured layer(s) and generates extensive coda wave trains that follow major seismic wave arrivals. The decay properties of these codas are affected by the planetary body's interior structure. To understand the propagation of seismic waves in such media, we model the transmission of seismic energy in highly scattering environments using an adapted phonon method. In this Monte Carlo simulation approach, we track a large number of seismic wavelets as they leave a source and we record the resulting ground deformation each time a wavelet reaches a surface receiver. Our method provides the first numerical global modeling of 3-D scattering, with user-defined power law distributions of scatterer length scales and frequency-dependent intrinsic attenuation, under the assumption of 1-D background velocity models. We model synthetic signals for simple, but highly scattering interior models and vary the model parameters independently to assess their individual effects on the coda. Results show that the magnitude of the decay times is most affected by the background velocity model, in particular the presence of shallow low-velocity layers, the event source depth, and the intrinsic attenuation level. The decay times are also controlled to a lesser extent by the size-frequency distribution of scatterers, the thickness of the scattering layer, and the impedance contrast at the scatterers.

## 1. Introduction

The study of seismic energy propagation in highly scattering bodies is a barely tapped field of planetary seismology research. Scattering of seismic energy occurs when coherent seismic wavefronts are randomly dispersed by a large number of small-scale heterogeneities. In environments with high levels of scattering, this process can obscure the arrivals of waves other than the *P* and *S* waves and thus limit the use of traditional analysis techniques that make use of body wave arrival times. The best, and only known nonterrestrial, example of this process is observed in the lunar Apollo Passive Seismic Experiment (APSE, 1969–1977) data. The recorded seismic waveforms are characterized by very long durations, by emergent onsets, and by the presence of very slowly decaying coda waves. These signals result from the interaction of seismic energy with the various velocity, attenuation, and scattering structures within the Moon and as such have the potential to reveal information regarding the lunar interior that is not accessible through more established seismological analyses. We showed in Blanchette-Guertin *et al.* [2012] that the manner in which scattered seismic signals decay can be used to assess first-order properties of the lunar interior structure. Our analyses of the APSE data indicated decay properties that are consistent with a shallow scattering layer comprising frequency-dependent scatterer number densities and scale lengths. However, these interpretations were restricted in part by the limitations of the APSE instruments (10 bit digitization and narrow bandwidth), but mostly by the lack of understanding of the processes governing seismic energy propagation in highly scattering media. Thus, in order to better appraise the interior structure of the Moon and other highly scattering bodies, we need to first understand the effects of varying velocity, attenuation, and scattering structures on seismic signal decay characteristics. In this paper, we address the following general questions: What impact does the seismic wave velocity profile have on the signals' coda (e.g., presence of a crust and of a very low-velocity layer, analogous to the surface regolith)? Can the decay properties of the seismic signals be used to assess the various scale lengths involved in the scattering

process (e.g., scattering layer thickness, overall properties of scatterer distributions)? Do deep structures like a small core have an impact on the coda wave trains? What happens to the seismic coda when scattering is not restricted to a near-surface highly scattering layer?

Investigation of seismic energy scattering in terrestrial environments started several decades ago. *Aki* [1969] made the first detailed analysis of coda wave trains, showing that these were generated by random heterogeneities in the terrestrial lithosphere. As such, seismic coda contains valuable information regarding the nature of the medium in which the energy propagated. Subsequent studies investigated seismic coda in order to assess lithospheric structures and material properties. For example, the strength of heterogeneities [e.g., *Aki and Chouet*, 1975; *Sato*, 1978] and the magnitude and temporal variations of the intrinsic attenuation factor [e.g., *Jin and Aki*, 1986; *Mayeda et al.*, 1992] can be measured with an analysis of the frequency content and amplitude decay properties of the scattered energy in seismic recordings. Several modeling approaches, all using a statistical treatment of scattering, have been developed to explain the characteristics of the scattered coda. Single-scatterer and multiple-scatterer models have been used in cases of low to moderate levels of scattering [e.g., *Aki*, 1969]. More intensively, scattering media necessitate other approaches like diffusion theory [e.g., *Latham et al.*, 1970b], the radiative transfer approach [e.g., *Margerin et al.*, 1998], or the modified phonon method presented in this work. The latter two are both based on generalized ray theory but implement the treatment of energy scattering differently. We explain below why we opted for an adapted phonon method for this work. A much more thorough review of seismic energy scattering theory and modeling approaches can be found in *Sato et al.* [2012] and *Yoshimoto and Jin* [2008], among others.

We present results from modeling of seismic coda in a highly scattering media, using a modified version of the Monte Carlo simulation method presented in *Shearer and Earle* [2004], in which a large number of seismic phonons are tracked as they travel through a planetary interior. The main advantages of this method are that it automatically generates single and multiple scattering events, it handles *P* to *S* wave and *S* to *P* wave conversions and effectively takes into account intrinsic attenuation. The phonon approach was initially used in seismological research work to model the envelopes of seismic waves of local earthquakes with epicentral distances in the tens of kilometers [*Gusev and Abubakirov*, 1987]. These quakes exhibit scattering characteristics that are much weaker than but qualitatively similar to those observed in lunar seismic events. The phonon method provided a new means to model seismic energy propagation in regions that could not be explained adequately with either the single scattering or the diffusion approximations. Adapted phonon methods were also used to investigate depth-dependent attenuation of coda waves [e.g., *Hoshiba*, 1994], to study the effect of increasing velocities with depth on the coda shape [e.g., *Yoshimoto*, 2000], to study the partitioning of wave energy in multiple scattering events [e.g., *Margerin et al.*, 2000], and to model the global short-period terrestrial wavefield (i.e., deep Earth scattering [see *Shearer and Earle*, 2004]). However, this method has not been used to simulate and investigate the effects of highly scattering environments such as the Moon on seismic signals, which is the main motivation behind this study. Our chosen modeling method effectively addresses the problem outlined in *Nakamura* [1977] regarding the synthesizing of seismic signals in highly scattering environments by providing a method to model both the diffusivity of seismic energy (high scattering levels) and simple body wave energy transmission.

We have adapted the *Shearer and Earle* [2004] method in two ways that are important for highly scattering environments: (i) 2.5-D ray tracing is used for scattered phonons, rather than pure two-dimensional (2-D) ray tracing, with probabilistic three-dimensional (3-D) heterogeneities. This is important for proper characterization of the scattering. (ii) Predetermined velocity and density heterogeneities can be incorporated directly in the model, in contrast to only stochastic perturbations. This can better characterize site effects due to scattering near the receiver when waveforms from all events undergo similar scattering from the same near-receiver structure.

We opted for this method, instead of other applicable techniques such as the radiative transfer method, because it makes minimal assumptions as to the detailed nature of the scattering media. The exact mechanical properties of the megaregolith, such as the nature and shapes of the scatterers, the length scales of scatterers, and the impedance contrast at the scatterers, are unknown. A more complex model which would require assumptions or extensive parameter searches regarding all of these properties and how they trade off with each other in terms of their observable effects on seismic coda. Given the inherent limitations of the lunar data set this trade-off space will be large. The method is also computationally

efficient for global scale models, even at high frequencies ( $\sim 10$  Hz). The limitations of our approach are that it is applicable only for highly scattering environments and does not explicitly model the physical scatterers. However, our goal is not to estimate the mechanical properties of the scattering material but instead to assess the effects of velocity and scattering structures on the generation and properties of lunar-like seismic codas.

An important aspect of our method that differs from previous modeling work [e.g., Przybilla *et al.*, 2009; Sato *et al.*, 2012] is that scatterers are modeled as interfaces, and not as points or small volumes. The orientation of each scatterer, as well as the impedance contrast at the interface, determines how the phonons deviate from their original path (i.e., by how much they are scattered). This method allows us to model the effect of a wide range of impedance contrasts. Other established techniques for modeling scattering (e.g., using the Born approximation) typically require that the velocity contrasts at the scatterers relative to the background-surrounding velocity are small [Sato *et al.*, 2012]. Scattering of seismic energy on the Moon mostly takes place in the near-surface scattering layer, known as the megaregolith. This layer is the product of billions of years of meteorite impacts on the lunar surface [Hörz, 1991]. In that layer, scattering occurs predominantly either at (i) the welded contacts between adjacent ejecta blocks, (ii) the interfaces between blocks of different lithologies (e.g., upper crust versus upper mantle, major faults bounding large craters and impact basins), or (iii) when seismic energy encounters high porosity where interfaces between blocks are not welded. We note that high porosity in the lunar uppermost crust is supported by data from the Gravity Recovery and Interior Laboratory mission and the recent work of Wiczorek *et al.* [2013]. In this context, the impedance contrasts caused by porosity or by adjacent varying lithologies are not always weak.

Our phonon method, dubbed PHONON1D because of its use of one-dimensional (1-D) velocity profiles, is described in detail in section 2. We have benchmarked our code against the TTBox [Knapmeyer, 2004] and the CRFL [Fuchs, 1968; Fuchs and Müller, 1971] packages for travel times, as well as against the CRFL package for amplitudes for synthetics computed in nonscattering environments (see section 3).

The goal of this work is not to produce synthetics that match the scattered properties of the APSE data. Our purpose is to build an understanding of the general consequences of interior structures of highly scattering bodies, like the Moon, on surface seismograms. Accordingly, we used the PHONON1D method to generate synthetic seismograms from shallow and deep sources in 16 different interior models with varying velocity, attenuation, and scattering properties. The resulting highly scattered waveforms can be characterized by their decay times ( $\tau_d$ ) and the frequency-dependent equivalent decay factor ( $Q_c$ ). We describe in section 4 the processing steps we followed to analyze the decay properties of the synthetic signals. We then present and compare examples of synthetic traces and decay properties for all the different models, and we follow with discussions on the effect of each model parameters (section 5).

## 2. Methodology

In our PHONON1D method, background  $P$  and  $S$  wave velocities ( $v_p$  and  $v_s$ ), density ( $\rho$ ), scattering probabilities ( $p_{sc}$ ), and intrinsic attenuations ( $Q_i$ ) are prescribed from 1-D (i.e., depth-dependent) models. The phonons travel in a 2-D disk, and at any given time a phonon's position is specified by its depth ( $z$ ) and epicentral distance ( $\Delta$ ). In order to capture the 3-D nature of scattering, randomly oriented scatterers can scatter phonons out of the plane of the 2-D disk by altering their azimuthal angle ( $\phi$ ). In this case, only the projection of the phonons' trajectories onto the 2-D disk is recorded. This method assumes longitudinal symmetry of the background models and the statistics of the scattering but allows us to model longitudinally scattered energy while only needing to track phonons on a 2-D disk.

### 2.1. Model Geometry

The phonons travel in a disk of radius  $R_M$ , where  $R_M$  is the radius of the planetary body under study. We use lunar-like dimensions (radius  $R_M = 1737$  km) in this work, mostly to save on computational requirements (the larger the body, the greater the number of phonons that have to be released) but also because the lunar seismic data set is to date the only one showing evidence of such high scattering intensity. Each phonon is released from a source located at  $\Delta = 0^\circ$ , at a specified source depth  $z_s$ . At each time step, the phonon's depth ( $z$ ), epicentral distance ( $\Delta$ ), and out-of-the-disk azimuth ( $\phi$ ) are recorded.  $\phi$  is initially set to  $0^\circ$  and changes only through the phonon's interaction with a scatterer. Such interactions can add an out-of-the-plane (longitudinal) component to the phonon's trajectory. In that case, for each time step, we project the phonon's path increment back onto the transmission plane such that only the colatitudinal ( $d\Delta$ )

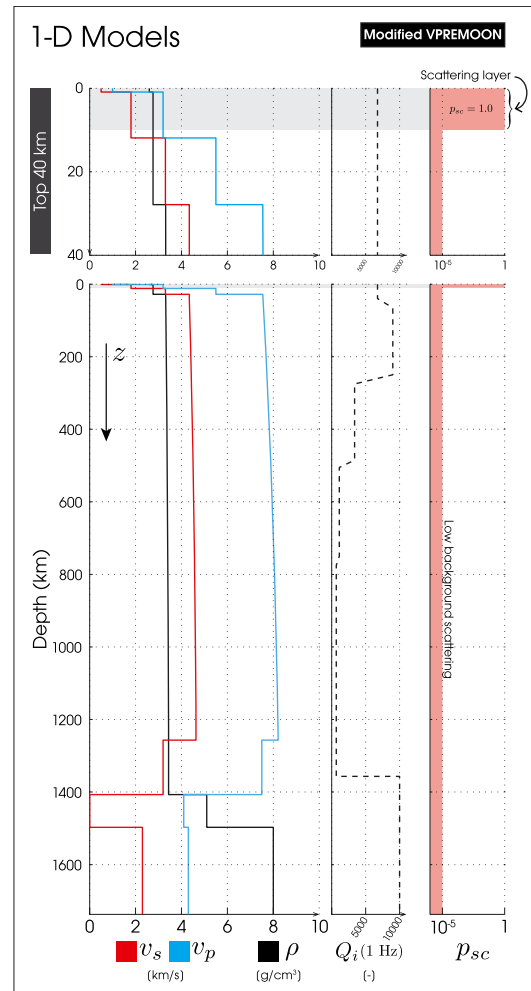


**Figure 1.** Example of a 1-D layered model:  $P$  and  $S$  wave velocities ( $v_p$ ,  $v_s$ ), density ( $\rho$ ), intrinsic attenuation for 1 Hz waves ( $Q_i(1 \text{ Hz})$ ), and the scattering probability ( $p_{sc}$ ). The modified VPREAMOON model shown here combines the crustal and mantle velocities from [Garcia et al., 2011] with the core velocities from [Weber et al. 2011]. This example model has a 10 km thick scattering layer ( $p_{sc} = 1$  near surface) and low overall background scattering ( $p_{sc} = 10^{-5}$  elsewhere). The top plot shows an expanded view of the upper 40 km.

occurs within the megaregolith layer, and for models that include background scattering beneath the main scattering layer, the background scattering is limited to depths shallower than 1000 km.

### 2.2. Velocity Profiles

The velocity profiles are specified as individual layers of up to 10 km thickness, separated by interfaces at which the layer properties (wave velocities, intrinsic attenuations, density, and scattering probability) are set. The properties of each layer are defined at the overlying interface. Layers of 0 km thickness define sharp boundaries (e.g., crust-mantle and core-mantle boundaries).

We applied the exact flattening transformation to each model interface [Bhattacharya, 1996, 2005]:

$$r/R_M = e^{-z_r/R_M} \tag{1}$$

$$v_p = (r/R_M)v_p^*, \quad v_s = (r/R_M)v_s^* \tag{2}$$

$$\rho = (R_M/r)^{p-2} \rho^* \tag{3}$$

and radial ( $dz$ ) components of displacement are recorded. For example, a phonon with an instantaneous azimuth of  $90^\circ$  (or  $270^\circ$ ) has no colatitudinal displacement (i.e., it remains at a constant  $\Delta$  over that time step, and until it is scattered again). This approach is justified by our assumption of longitudinal symmetry. In this context, any phonon that leaves the transmission plane ( $\phi \neq 0^\circ$ ) is assumed to be replaced by a phonon entering the plane from the opposite direction. Thus, any phonon with a nonzero azimuth can be considered equivalently as scattered energy that enters or exits the plane. This aspect of the model is required to capture the 3-D nature of scattering. Nonscattered phonons have a constant  $\phi = 0^\circ$ , and they propagate purely in the transmission disk (2-D propagation). The model geometry is illustrated in Figures 1 and 2.

In a sphere, out-of-plane energy will sample velocities at a different radius than energy projected back into the plane of the 2-D disk. This is important if the energy travels a large distance out of the plane and/or if the curvature of the spherical shell at that radius/depth is large, i.e., the difference between the projected in-plane and the out-of-plane radii and hence the difference in velocities increases with depth. However, one can minimize this effect by only using small time steps (short distances) before reevaluating the phonon's velocity. In our case, the phonon will travel a maximum distance of 10 km out of the plane (and typically only tens to hundreds of meters given our distribution of distances between scatterers) before we reassess its radial position and the corresponding velocity. This results in a maximum error in radius of 10 km, if the phonon travels directly perpendicular to the transmission disk ( $\phi = 90^\circ$ ), and very close to the core. This error decreases dramatically at shallower depths, and is negligible at depths throughout the lunar crust and mantle. In our work, most of the scattering

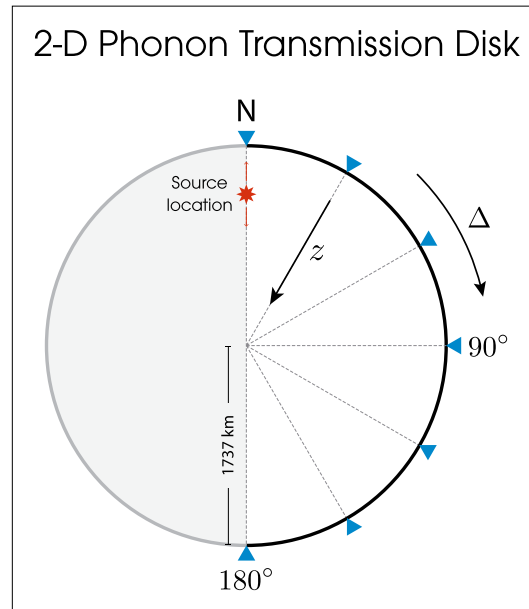


**Figure 2.** Phonons travel in a 2-D disk of radius  $R_M$  ( $R_M = 1737$  km). The phonon depth ( $z$ ) and epicentral distance ( $\Delta$ ) are tracked at each time step. Phonons that reach the surface are recorded by receivers (blue triangles) spaced at regular intervals along the surface away from the source (located at  $\Delta = 0^\circ$ ). Phonons are allowed to travel to distances greater than  $180^\circ$ . They are, however, reflected back into the  $0$ – $180^\circ$  half disk if they reach the surface.

where  $r$  is the distance from the center of the planetary body to the interface,  $R_M$  is the radius of the planetary body,  $z_f$  is the transformed depth coordinate,  $v_p^*$  and  $v_s^*$  are the original  $P$  and  $S$  wave velocities,  $v_p$  and  $v_s$  are the transformed  $P$  and  $S$  wave velocities,  $\rho^*$  and  $\rho$  are the original and transformed densities, and  $p$  is an arbitrary constant that varies with wave type [Bhattacharya, 1972, 1996]. In this work,  $p$  is set to  $-2$ , as in Bhattacharya [2005].

The flattening transformation results in a singularity at the core ( $r = 0$  km). To avoid numerical error during the calculation of the phonon path, we assume that any phonon that travels to within  $0.1$  km of the center of the planetary body travels through the center point, and we adjust the travel time ( $dt = 0.2/v_{\text{core}}$ , where  $v_{\text{core}}$  is the seismic wave speed in the core in km/s) and epicentral distance ( $d\Delta = \pi R$ ) accordingly.

### 2.3. Seismic Source

We use a modified simple analytical two-sided pulse [Dahlen, 2005] as a source function for quakes (source depth  $z_s > 0$  km), defined as

$$m(t) = -4\pi^2 P_0^{-2} (t/3 - P_0/2) e^{-2\pi^2 (t/3P_0 - 1/2)^2}, \quad (4)$$

where  $m$  is the source function,  $t$  is time,  $P_0 = 4\Delta t$ , and  $\Delta t$  is the signal sampling interval. The equation was modified from the original in order to introduce more low frequency energy. The focal mechanisms of nonterrestrial quakes are still poorly understood, and so we use a circular radiation pattern in our modeling work. However, the radiation pattern could be adjusted to fit any particular focal source. For a circular radiation pattern, the release angle is a uniform random number between  $-\pi/2$  and  $\pi/2$ , where  $0$  is horizontal,  $-\pi/2$  is upward, and  $\pi/2$  is downward. The phonon's polarity at the source is randomly determined based on a energy partitioning ratio of 1:10:10, for  $P$ ,  $SV$ , and  $SH$  waves, respectively [Boatwright and Fletcher, 1984]. In the case of impact events ( $z_s = 0$  km), the source function is a delta function with release angles randomly selected between  $0$  and  $\pi/2$  (downward direction only). Only  $P$  wave energy is released for such events; i.e., the energy partitioning ratio is set to 1:0:0. The initial ray parameter ( $p$ ) is set at this stage, based on the release angle, polarization, and corresponding velocity at the source depth. If the scattering probability ( $p_{sc}$ ) is set to  $0$ , then  $p$  remains unchanged as the phonon travels throughout the Moon.  $p$  will change if the phonon is scattered by a nonhorizontal scatterer. Sources used for the synthetics shown in the modeling section (section 4) are presented in Figure 3, along with the corresponding power spectra. We used a sampling frequency of  $40$  Hz (i.e.,  $\Delta t = 0.025$  s) for all synthetic signals presented in this article.

### 2.4. Scattering Layers

If a phonon reaches a layer in which the scattering probability is greater than  $0$  ( $p_{sc} > 0$ ), it will travel within that layer, from scatterer to scatterer, until it reaches the next velocity interface or until it is sent back to the initial interface if it is backscattered. The distance between scatterers ( $\delta_{sc}$ ) can be set to a constant value (e.g., we use  $10$  km for global background scattering) or can be stochastically selected from a power law probability distribution ( $\delta_{sc}^{-n}$ ) where small interscatterer distances have a higher probability of occurrence than large distances (as in Figure 4). A power law distribution for megaregolith blocks is motivated by the heterogeneity length scales generated by impactors of different sizes [e.g., O'Keefe and Ahrens, 1987]. In this work  $n$  is always equal to  $0.5$ . Further investigations could study the effect of various  $n$  values, or different length scale probability distributions (e.g., uniform distribution, only one  $\delta_{sc}$  values, etc.)

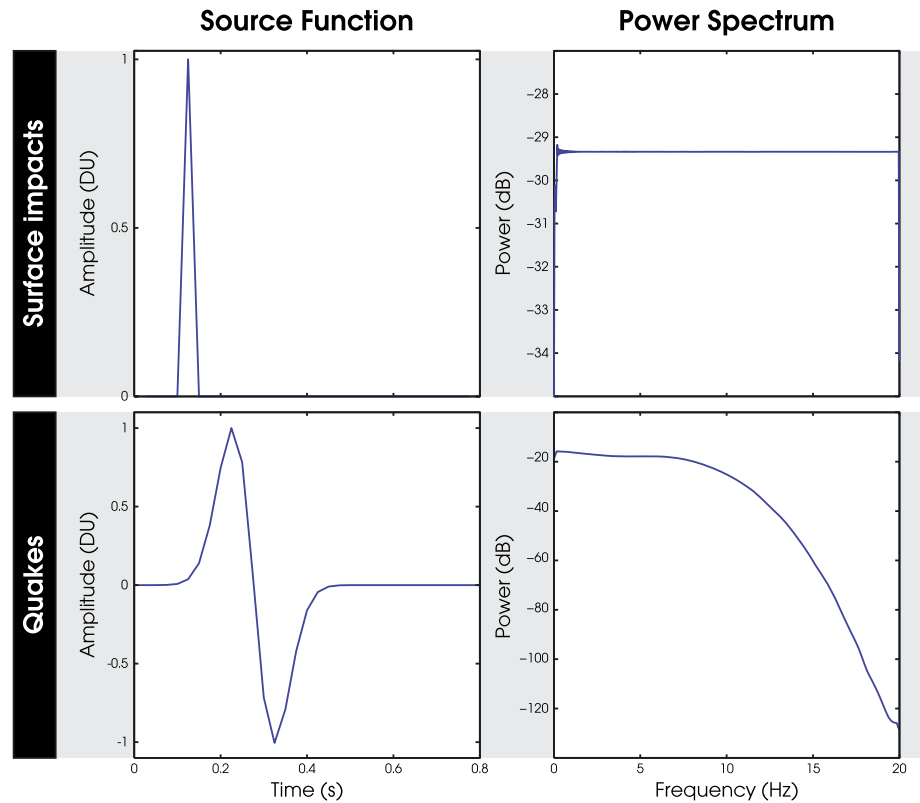


**Figure 3.** Source functions, in digital units (DU), used in the modeling for (top row) impact events and (bottom row) quakes. (right column) The corresponding power spectra. A sampling frequency of 40 Hz was used throughout.

Once a phonon reaches a scatterer, it is scattered, or not, based on the scattering probability. Let  $r_x$  be a random number between 0 and 1 taken from a uniform distribution, where different subscripts,  $x$ , indicate different random numbers as described below. If  $r_1 > p_{sc}$ , the phonon is not scattered; if  $r_1 < p_{sc}$ , scattering occurs. In that case, a random scatterer orientation and velocity/density perturbations are generated and the phonon will be reflected or transmitted with a probability based on the reflection/transmission coefficients as for conventional ray theory at a solid-solid interface (Figure 5b and section 2.5). The

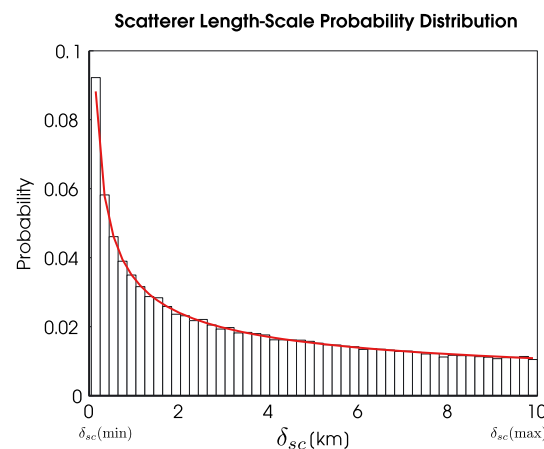


**Figure 4.** Scatterer length scale probability distribution. The distance a phonon will travel between two consecutive scatterers is randomly picked from the power law distribution such that a phonon will travel a greater number of short distances ( $\delta_{sc}(\min)$ ) than large distances ( $\delta_{sc}(\max)$ ).

orientation of the scatterer (dip between 0 and  $\pi/2$ , where 0 is locally horizontal and  $\pi/2$  is vertical and strike between 0 and  $2\pi$ ), as well as the magnitude of the perturbations ( $\pm r_2 \delta v_{p/s}$  and  $\pm r_2 \delta \rho$ , where  $\delta v$  and  $\delta \rho$  are the maximum change in velocity and density at the scattering interface, see Figure 5b) will define the orientation of the scattered phonon via its incident and azimuth angles. In our models the orientations of the scatterers are selected such that the vectors normal to the scattering interfaces are uniformly distributed (strike is defined as  $r_3 2\pi$ , and the dip as  $\sin^{-1} r_4$ ). Also, the maximum  $\delta v$  and  $\delta \rho$  perturbation levels are kept equal and is referred to as  $\delta_{v,\rho}$ . Once the phonon has interacted with the scatterer, it travels a new random distance  $\delta_{sc}$  to the next scatterer. If  $\delta_{sc}$  is larger than the distance between the phonon and the next velocity interface, the phonon travels directly to the

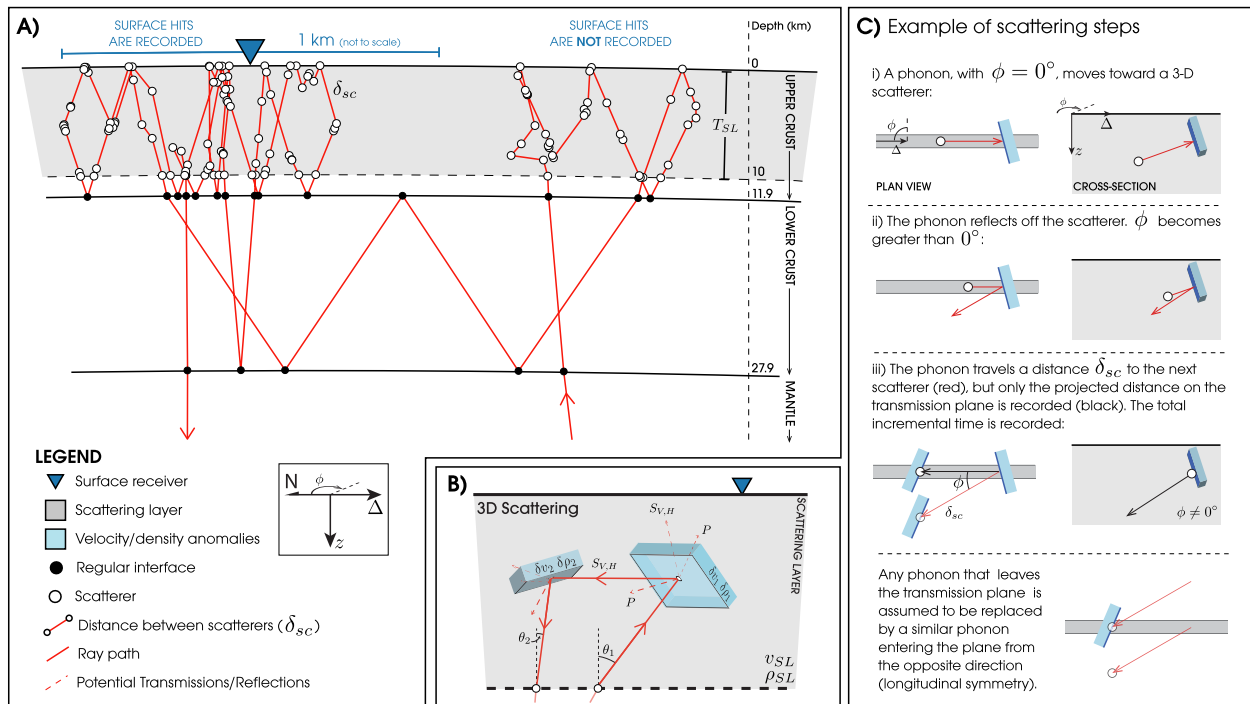


**Figure 5.** (a) Example of a scattered raypath in a 10 km thick surface scattering layer. The red line shows the path of the phonon as it enters and leaves the scattering layers. The white dots represent the 3-D scatterers. Inset shows angle  $\phi$  which is nonzero when the phonon has an out-of-plane component. (b) Randomly oriented 3-D scatterers, represented here as interfaces with different impedance values from the background values. The probability that the incident ray will be reflected or transmitted, as  $P$ ,  $SV$ , or  $SH$  energy, is proportional to the square of the reflection/transmission coefficient. Due to the 3-D nature of the scatterer, the phonon can acquire an out-of-the-plane component ( $\phi \neq 0^\circ$ , not shown here). (c) Example scattering steps showing a change in the azimuthal angle ( $\phi$ ).

velocity interface. Because of the 3-D geometry of the scatterers, and depending on the phonon's incident and azimuthal angles, scattering can convert the phonon's polarity to  $P$ ,  $SV$ , or  $SH$  energy (e.g., Figure 5b). The transmission and reflection coefficients are calculated with the same equations that govern the behavior of phonons at regular interfaces (next section).

In the modeling work presented in section 4, the scattering probability in the scattering layer ( $\rho_{SL}$ ) is always set to 1, such that phonons will always interact with the scatterers. In this case, the intensity and overall direction of scattering are controlled by the impedance contrast at the scatterer (i.e., the differences in velocity and density between the scatterers and the background values,  $(\delta_{v,\rho})$ ). As the average impedance contrast approaches 0 ( $r_2 \delta_{v,\rho} \rightarrow 0$ ), most phonons will be scattered forward (transmission is favored over reflection) with only a small deviation from their original path, regardless of the orientation of the scatterers. Scattering outside of the near-surface scattering layer can be set by setting the global scattering probability ( $\rho_G$ ) to a nonzero value. Global scattering is limited to depths shallower than 1000 km in the models presented in section 4.

Using variable distances between scattering events ( $\delta_{sc}$ ), as well as a range of impedance contrasts, allows us to implement a frequency dependence of the coda decay without having to model the detailed nature of the scatterers. This is illustrated in Figure 6 for two simple cases. In Figure 6a, scattering events occur close to each other (short  $\delta_{sc}$ ) and the impedance contrast at each event is low such that a discretized gradient forms between region of  $v_1$  and  $v_2$ . In an ideal case, if a large number of phonons are released from the source, many phonons go through a similar path and encounter similar scatterers. At each scattering event, some of the energy (i.e., phonons) is transmitted forward, and some is reflected back toward the receiver. The reflections occur at different depths and distances such that the phonons reaching the receiver are spread in time and space. This generates constructive or destructive interferences that affect the amplitude and frequency content of the recorded signals. In Figure 6b, the distance between the scatterers and the impedance contrasts are large such that the scatterers act more as interfaces than gradients. In this case, phonons with similar initial directions are transmitted and reflected along two similar paths and generate

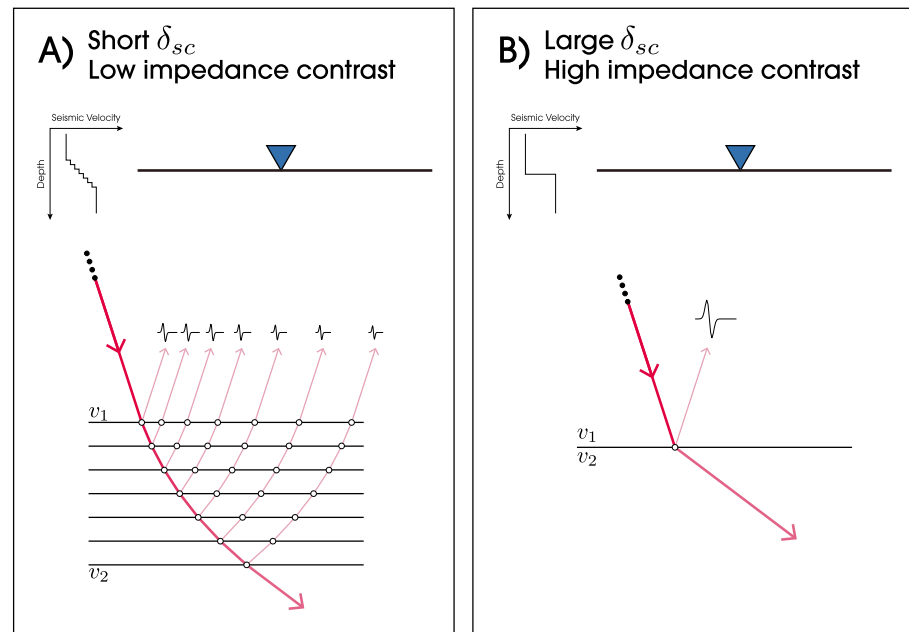


**Figure 6.** (a) Scattering events occur close to each other. The impedance contrast at each event is low such that a gradient forms between region of velocities  $v_1$  and  $v_2$ . In an ideal case, if a large number of phonons are released from the source, many phonons will travel along a similar path and encounter a similar (but not exactly the same) distribution of scatterers. At each scatterer, some of the energy (i.e., phonons) will be transmitted forward, and some will be reflected back toward the receiver. The reflections occur at different depths and distances such that the phonons reaching the receiver will be spread in time and space. This generates constructive or destructive interferences that in turn determine the amplitude and frequency content of the recorded signals. (b) Both the distance between the scatterers and the impedance contrasts are large such that the scatterers act as interfaces rather than as gradients. In this case, phonons with similar initial directions will be transmitted and reflected along two similar paths and will generate a much more impulsive wavelet at the receiver.

a more impulsive wavelet at the receiver. Implementing frequency dependence this way allows us to make minimal assumptions regarding the properties of the scatterers (and trade-offs among those properties) while adequately matching the frequency dependence of scattering that can be observed in highly scattering environments such as on the Moon.

### 2.5. Regular Velocity Interfaces

When a phonon reaches an internal boundary, the likelihood that it reflects or transmits in a particular polarization is proportional to the square of the amplitude reflection or transmission coefficient normalized by the sum of the squares of all coefficients. A random number is generated to determine the state of the scattered phase. The phonon will then travel to the next interface if the layer's scattering probability is 0 ( $p_{sc} = 0$ ), or to the next scatterer, if  $p_{sc} > 0$ .

The coefficients are calculated based on the incoming phonon's incident angle and polarity. Coefficients for solid-solid interfaces are based on *Aki and Richards* [2009], whereas those for the free-surface reflections and solid-liquid interfaces come from *Ben-Menahem and Singh* [1981]. Benchmarking of wave amplitude with the CRFL package (section 3) showed that results are better when we conserve energy rather than amplitude at the interfaces. Hence, we use the square of the amplitude coefficients, normalized by the sum of the squares.

All coefficients acquire an imaginary component if any of the transmission or reflection angles are supercritical ( $v_{(p,s)}p > 1$ , where  $p$  is the ray parameter). In this case, we set the coefficient(s) with the supercritical angle to 0 (based on *Ben-Menahem and Singh* [1981]) and use the moduli of the other complex coefficients.

### 2.6. Surface Recorders

Seismometers are distributed at specific intervals along the surface and record the radial, transverse, and vertical ground displacements each time a phonon comes within a prescribed distance, set to 1 km in this

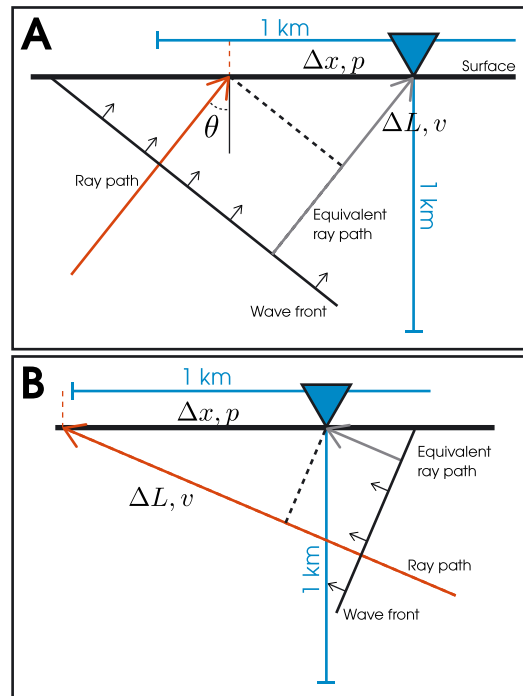


**Figure 7.** All phonons that pass within 1 km (a) horizontally or (b) vertically of a receiver before hitting the surface are recorded, whether they hit the surface within 1 km of the receiver (Figure 7a), or not (Figure 7b). In all cases, a time correction ( $\Delta t$ ) is applied. We assume that the phonon's path (red arrow) is perpendicular to the corresponding planar wavefront. This phonon travels a distance that is different by  $\Delta L$  km from the distance traveled by a similar phonon (gray arrow) hitting the surface directly underneath the receiver at a velocity of  $v$  km/s. The resulting time difference ( $\Delta t$ ) is equal to the horizontal slowness ( $p$ ) multiplied by the distance difference at the surface ( $\Delta x$ ) and must be subtracted or added from the arrival time of the phonon that reaches the surface away from the receiver.

attenuation factor ( $Q_i$ ) at the depth at which a given travel time increment was spent. For each time step, we record the incremental time spent in a layer with a given  $Q_i$ , and  $t^*$  is the sum of these incremental attenuations.

### 3. Modeling Method Benchmarking

As there are no standard numerical benchmarks against which to compare our scattering phonon code, we benchmarked the travel times and amplitude of synthetic signals generated in nonscattering environments. The assumption is that synthetics generated in highly scattering media will have coda with realistic rise and decay characteristics if the amplitudes and times for nonscattered signals have been shown to be appropriate.

We benchmarked the PHONON1D code against the TTBox package [Knapmeyer, 2004] for travel times, and against the reflectivity CRFL code [Fuchs, 1968; Fuchs and Müller, 1971] for both travel times and wave amplitudes. The PHONON1D synthetics match the TTBox and CRFL travel times, for both terrestrial (Figure 8a) and lunar (Figure 8b) models. Wave amplitudes (Figures 8b and 8c) compare well for direct waves, but small discrepancies between synthetics from the PHONON1D and CRFL codes are seen at larger times, after the seismic energy has undergone multiple reflections and refractions. We briefly explain below why these discrepancies arise and why the benchmarking results indicate that our code is adequate to be used for its intended purpose of computing synthetics in highly scattering media.

work, from a receiver. Different receiver dimensions (between 1 and 2.5 km) produce similar decay times, and signal amplitudes differ proportionally given that less or more phonons are recorded at each stations for various receiver dimensions. We correct for time if the phonon does not hit the surface directly beneath the receiver (Figure 7). The applied correction,  $\Delta t$ , is

$$\Delta t = \frac{\Delta L}{v} = \frac{\Delta x \sin \theta}{v} = p \Delta x, \quad (5)$$

where  $\Delta L$  is the additional distance the phonon would have traveled if it had hit the surface directly beneath the receiver,  $v$  is the wave speed,  $\Delta x$  is the distance between the receiver and the arrival position of the phonon on the surface,  $\theta$  is the ray incident angle, and  $p$  is the ray parameter.  $\Delta t$  is negative when the phonon hits the surface before the receiver (Figure 7a) and positive when it hits the surface past the receiver (Figure 7b). The resulting  $\Delta t$  is also used to calculate the correction to the phonon's attenuation.

### 2.7. Intrinsic Attenuation

We calculate the attenuation of the phonon's amplitude as follows:

$$A(\omega) = A_0 e^{-\omega t^*}, \quad (6)$$

$$t^* = \sum \frac{\Delta t}{Q_i(z)} \quad (7)$$

where  $A$  is the recorded amplitude at time  $t$ ,  $A_0$  is the phonon's initial amplitude (typically, 1 digital unit (DU)),  $\omega$  is the angular frequency, and  $Q_i(z)$  is the depth-dependent intrinsic attenuation factor. We track each phonon's  $t^*$ , which is the sum of all time increments traveled divided by the

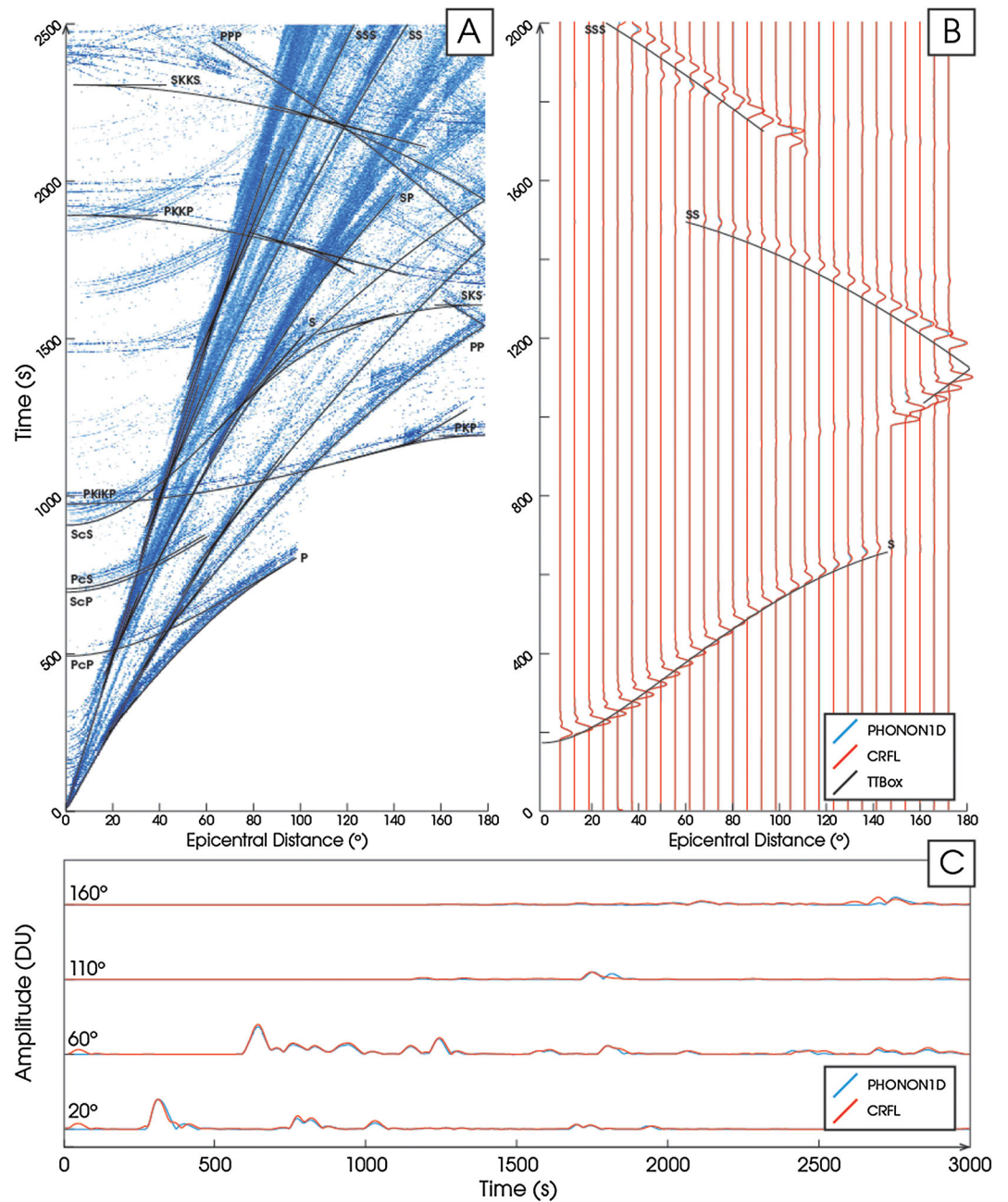


**Figure 8.** (a) PHONON1D synthetics (blue) versus TTBox travel times (black), for a PREM model, with a 100 km depth point source. The logarithm of the wave amplitudes is plotted in order to show weaker wave arrivals at later times. We only show travel times that TTBox can compute (i.e., not all multiple reflection phases at later times are identified). (b) Comparisons between PHONON1D traces (blue) and CRFL traces (red), showing the transverse component (no *P* wave energy) in the 0.10–0.15 Hz frequency band. This is for a simple two-layered Moon, with a 700 km depth point source. Black lines are TTBox arrival times. (c) Comparisons between PHONON1D traces (blue) and CRFL traces (red), for a PREM model, with a 100 km depth source, showing the vertical component in the 0.10–0.15 Hz frequency band. The PREM model has many interfaces and the discrepancies between the two codes get larger at larger times (e.g., 160°). Note for that both Figures 8b and 8c, CRFL plots on top of the phonon code traces, so the absence of blue means a good fit.

The reflectivity method allows a quick estimation of the reflected and transmitted wave field as a function of frequency, ray parameters, and distances [Fuchs, 1968]. The CRFL code was constructed using wave theory in layered media, which is intrinsically different from the PHONON1D approach itself based on generalized ray theory. For example, CRFL computes all wave phase shifts at interfaces, whereas PHONON1D only tracks

**Table 1.** Models Investigated in This Study<sup>a</sup>

Model	1-D Velocity Model	$T_{SL}$ (km)	$\delta_{v,\rho}$ (%)	$Q_i(1 \text{ Hz})$ (-)	$Q_i(f)$ Style	$p_G$ (%)	$\delta_{sc}$ (km)	
							min	max
A	Constant velocity	30	75	4500	1	0	0.05	10
B	Constant velocity	15	75	4500	1	0	0.025	5
C1	Crust	30	75	4500	1	0	0.05	10
C2	VLVL	30	75	4500	1	0	0.05	10
C3	VPREMOON	30	75	$Q_i(z)$	2	0	0.05	10
D1	Constant velocity	5	25	4500	1	0	0.05	10
D2	Constant velocity	5	75	4500	1	0	0.05	10
D3	Constant velocity	5	95	4500	1	0	0.05	10
D4	Constant velocity	60	25	4500	1	0	0.05	10
D5	Constant velocity	60	75	4500	1	0	0.05	10
D6	Constant velocity	60	95	4500	1	0	0.05	10
E	Solid core	30	75	4500	1	0	0.05	10
F	Constant velocity	30	75	4500	2	0	0.05	10
G1	Constant velocity	30	75	2000	1	0	0.05	10
G2	Constant velocity	30	75	6500	1	0	0.05	10
H	Constant velocity	30	75	4500	1	0.01	0.05	10

<sup>a</sup> $T_{SL}$  is the scattering layer thickness,  $\delta_{v,\rho}$  is the maximum velocity and density perturbation level at each scatterer, and  $Q_i(1 \text{ Hz})$  is the reference intrinsic attenuation. The different  $Q_i(f)$  styles are plotted in Figure 10.  $p_G$  is the low-level global scattering probability, and  $\delta_{sc}$  sets the minimum and maximum scatterer length scales, as defined in Figure 4. Model A is the baseline model, with constant  $P$  and  $S$  wave velocities, a scattering layer thickness of 30 km, maximum velocity and density perturbations at the scatterers of  $\pm 75\%$ . For model C3,  $Q_i = Q_i(f, z)$  and  $Q_i(1 \text{ Hz})$  is depth dependent and is plotted in Figure 1.

the 90° shifts occurring at caustic points (e.g., we do not track diffuse waves). We chose to not implement extensive phase shift tracking in order to keep the computation costs to a minimum. Nonetheless, we have opted to benchmark our code with CRFL because it allows us to compare synthetics at higher frequencies than other codes easily allow (e.g., SPECIFEM and MINEOS). It is thus reasonable to expect an imperfect match between synthetics from both codes, especially for more complicated velocity profiles (e.g., terrestrial profiles versus our simple lunar profiles). The criteria we used to decide if benchmarking was satisfactory were (i) good visual fit of travel times, (ii) good visual fit of primary wave amplitudes, and (iii) the difference between the seismograms from the two models is less than 10%. All benchmarking runs met these three criteria, except for the preliminary reference Earth model (PREM) seismograms at large epicentral distances ( $> 110^\circ$ ) for which the difference with the CRFL signals can reach 20%. This is explained by the fact that at these distances, the amplitudes of the main arrivals are lower, seismic energy is more spread out, and the contribution of waves that are not modeled by the PHONON1D method (e.g., core diffracted waves) is larger.

The PHONON1D code was not built to study seismic waves in a nonscattering environment. CRFL, or other packages, is better suited to do so. The code's main purpose is to study the propagation of seismic energy in highly scattering media at larger frequencies (up to  $\sim 10 \text{ Hz}$  in this work). In such an environment, most of the nonprimary wave types ( $PP$ ,  $SS$ ,  $SP$ ,  $PcS$ , and so on) will be very low amplitude and are hidden by the  $P$  and  $S$  wave scattered coda, as observed in the APSE data.

#### 4. Modeling Approach

Using the PHONON1D code, we computed synthetic signals in 16 distinct highly scattering planetary interiors. We present this modeling work and the results in this section. We focused our investigations on seven different model parameters: specific 1-D velocity and density profiles, the thickness of the near-surface scattering layer ( $T_{SL}$ ), the maximum velocity and density perturbation levels at each scatterer ( $\delta_{v,\rho}$ ), the reference intrinsic attenuation ( $Q_i(1 \text{ Hz})$ ), the intrinsic attenuation frequency dependence ( $Q_i(f)$ ), the probability of low-level global scattering ( $p_G$ ), as well as the minimum and maximum scatterer length scales ( $\delta_{sc}$ ). Most of the velocity profiles used are very simple, the majority having constant  $P$  and  $S$  wave velocities throughout the body. Some of these velocity profiles are somewhat unrealistic but were chosen

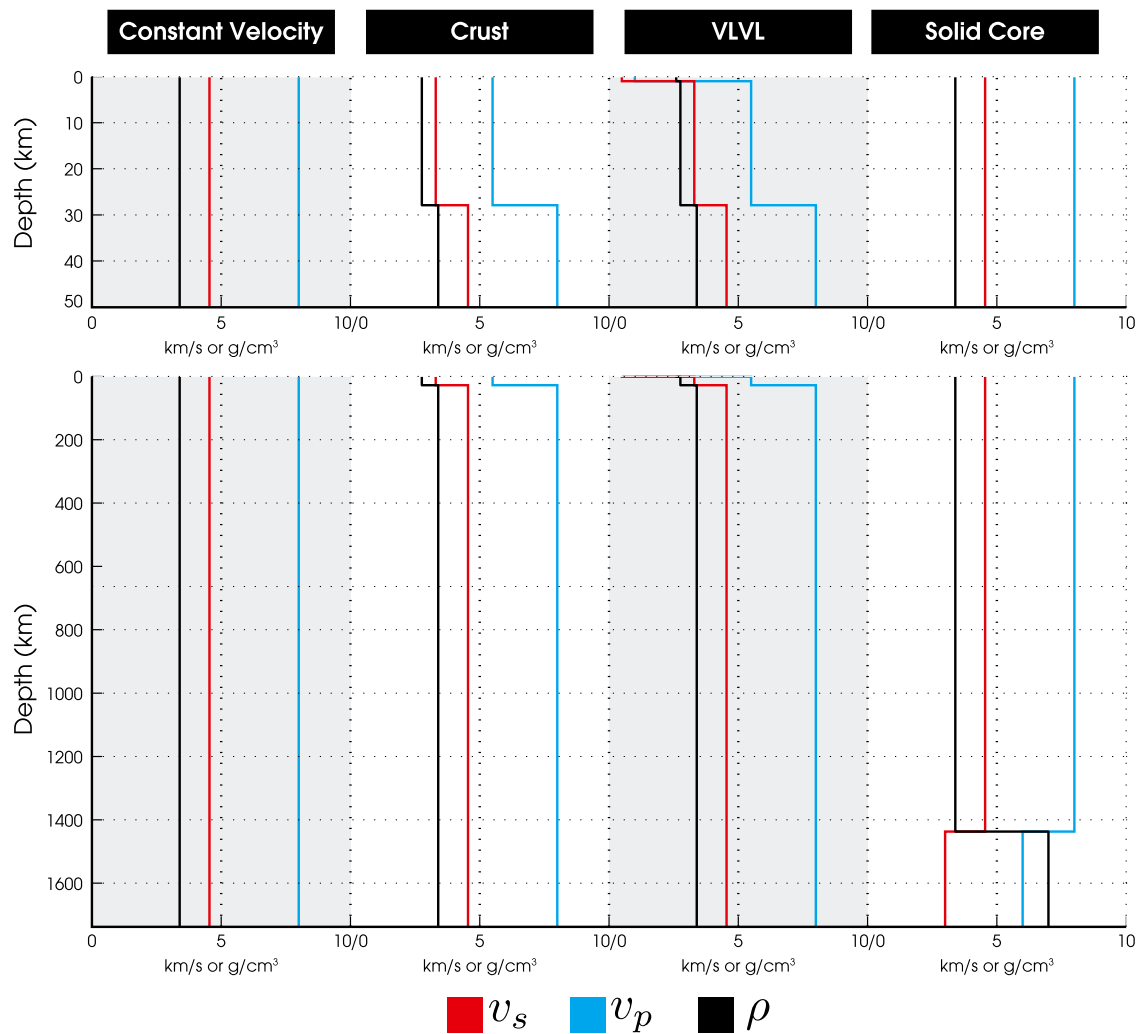


**Figure 9.** Four of the five 1-D velocity and density profiles used in this study, showing the  $S$  wave velocity (red), the  $P$  wave velocity (blue), and the density (black). The modified VPREAMON profile used in C3 is shown in Figure 1.

for their simplicity and to allow us to easily investigate the individual effects of each model parameter on the seismic coda.

The parameters for all models are outlined in Table 1. Figures 1 and 9 show the five 1-D velocity and density profiles used. Model A is defined as the baseline model, and all other models implement simple variations from it. Other models have been grouped using sequential model names (e.g., C1, C2, and C3) in order to indicate which models are used to demonstrate the effect of a specific velocity, attenuation or scattering structure on the coda. Note that the background intrinsic attenuation factor,  $Q_i(f)$ , is high when compared to typical terrestrial values (i.e., much lower attenuation levels), but this is necessary to obtain synthetics with long scattered coda. Such high  $Q_i$  values can be expected in very dry planetary environments [e.g., Latham *et al.*, 1970a; Nakamura *et al.*, 1976].  $Q_i(f)$  is kept constant at 2000, 4500, or 6500 in most models but increase with increasing frequencies in models C3 and F (Figure 10).

We computed synthetics for events at three distinct depths: surface events ( $z_s = 0$  km), shallow events ( $z_s = 30$  km), and deep events ( $z_s = 1000$  km). These are analogous to surface impacts, lunar shallow quakes, and lunar deep quakes, respectively. The resulting decay properties of the shallow events are very similar to these of the surface impacts. This is a result of the sources being located in, or very near the surface scattering layer in both cases. Thus, we only present the synthetic traces and decay analysis results from the surface impacts and deep events. As mentioned earlier, we used lunar-like dimensions for this particular

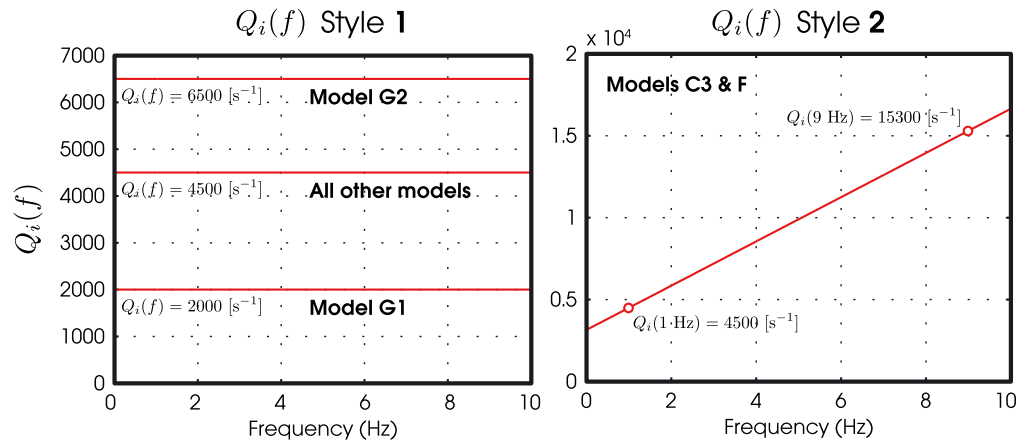


**Figure 10.** The two different  $Q_i(f)$  styles used in the modeling work. Style 1 has a constant  $Q_i$  over the entire frequency range. Most models use  $Q_i(f) = 4500$ , except for models G1 ( $Q_i(f) = 2000$ ) and G2 ( $Q_i(f) = 6500$ ). Style 2 has increasing  $Q_i$  for increasing frequency:  $Q_i(1 \text{ Hz}) = 4500$ , up to  $Q_i(9 \text{ Hz}) = 15300$ . Style 2 is used in models C3 and F.

work (planetary radius of 1737 km). However, this method could be applied to much larger (i.e., Mars) or smaller (e.g., asteroids) bodies.

#### 4.1. Processing of Synthetics

We used a method similar to the one described in *Blanchette-Guertin et al.* [2012] to measure the characteristic decay time ( $\tau_d$ ) and decay factor ( $Q_i$ ) of the synthetic signals. All synthetic data were band-pass filtered to allow the measurement of the decay properties in specific frequency bands. For this study, we investigated decay properties in five 2 Hz wide bands centered on 1, 3, 5, 7, and 9 Hz. We then computed the signals' envelope functions and smoothed them in order to reduce the contribution of noise spikes in the decay fits. Smoothing was done by using a 35 s running window, keeping the 75th percentile. The decaying part of the smoothed curves were fitted in a least squares sense with an exponential decay curve of the form  $e^{-t/\tau_d}$ , and  $\tau_d$  was retrieved [see *Blanchette-Guertin et al.*, 2012, Figure 3]. The coda wave decay factor  $Q_c$  was then calculated using

$$Q_c = 2\pi f_c \tau_d \tag{8}$$

where  $f_c$  is the central frequency of the band of interest.  $Q_c$  is useful to compare decay properties in different frequency bands. Its inverse,  $Q_c^{-1}$ , represents the fraction of energy dissipated after one period of oscillation. In a closed system with uniformly distributed energy, the signal amplitude decay factor  $Q_c$  should be controlled by, and equal to, the intrinsic attenuation factor  $Q_i$ .  $Q_c$  values that are less or more than the local  $Q_i$  suggest leaking or focusing of seismic energy away from or toward the receiver.

The beginning of the fits were determined automatically as the time at which the energy starts to decay exponentially after the theoretical S wave arrival time. In some models with lower levels of scattering not all the energy from the impulsive wave arrivals is converted into the scattered coda. Fitting only the exponentially decaying part of the coda ensures that we do not fit the larger amplitude impulsive arrivals and retrieve artificially low decay times. It follows that the decay times and decay factors discussed in the following sections are the S wave coda decay times and factors. All S wave travel times were computed using the TTBox package [Knapmeyer, 2004]. The  $\tau_d$  values for individual radial, vertical, and transverse components were similar in all cases and only the average  $\tau_d$  values from all three channels are shown here. Fits were of an arbitrarily determined length of 2500 s and were only retained if  $\tau_d$  was less than 2500 s. Most fits fell within that constraint and only a small number of fits for models with high scattering levels were dropped.

### 5. Results and Discussion

Figure 11 presents examples of synthetic traces from all models, for surface impacts and deep events, recorded at an epicentral distance of 50°. All traces have been normalized by their maximum amplitude for

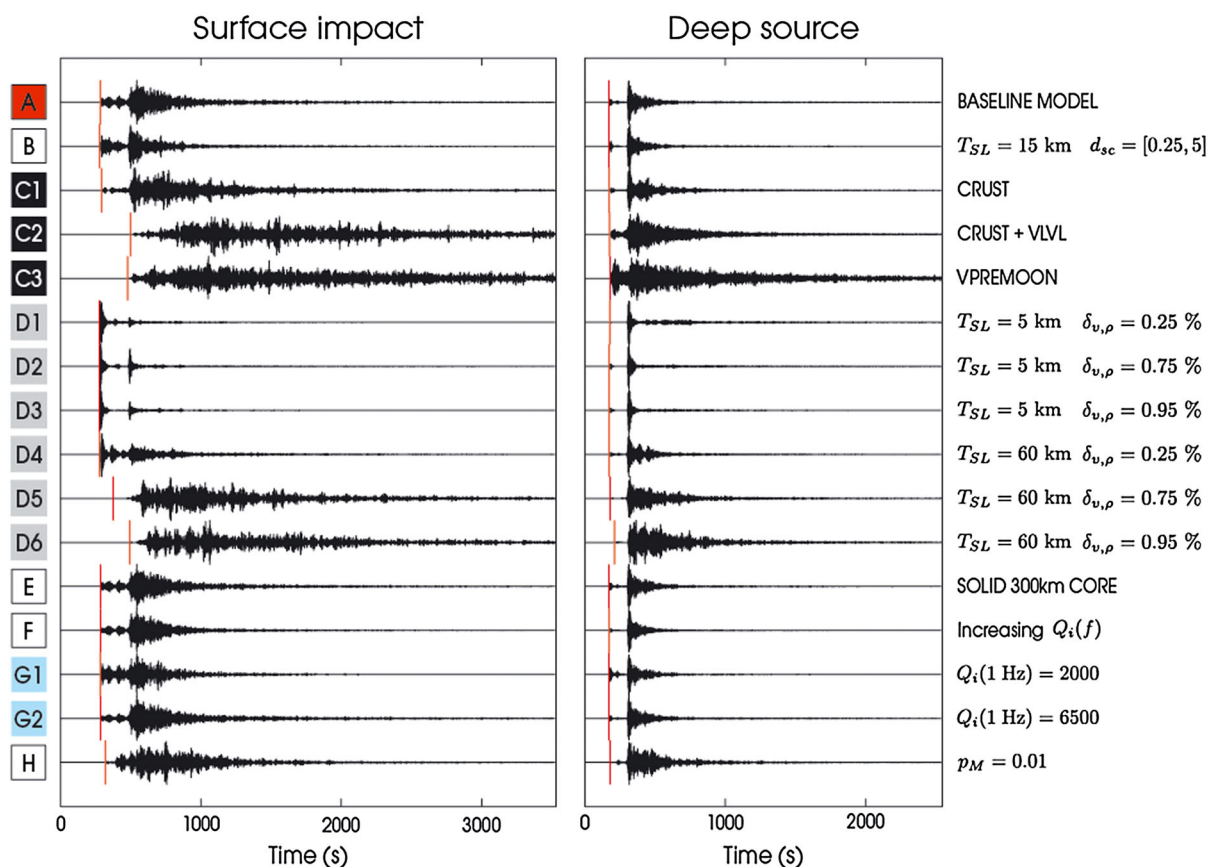


**Figure 11.** Examples of synthetic traces for all models presented in this work, for both surface impacts and deep event, at  $\Delta=50^\circ$ . Note that amplitudes can vary greatly among models, so the traces have been normalized such that their maximum amplitudes are equal. All traces are aligned on the theoretical  $P$  wave arrival times. The top traces are from the baseline model (model A). For each other models (B to H), the annotation on the right indicates the main difference(s) with respect to the baseline model. A detailed description of all the models, including the symbol definitions, can be found in Table 1. The red lines indicate the time of the first  $10^{-7}$  DU hit for each traces, which is not the theoretical  $P$  wave arrival time, but the first time at which enough phonons hit the receiver to trigger the minimum  $10^{-7}$  DU amplitude signal. The choice of label colors is arbitrary and designed only to accentuate the different model groupings. Models with white labels are those that can be used individually to show the effect of a particular model parameter.

better visualization and are aligned on the theoretical  $P$  wave arrival times. The thin red lines indicate the time of the first  $\pm 10^{-7}$  DU hit, i.e., the first *observable*  $P$  wave arrival.  $10^{-7}$  DU is the minimum amplitude output by the code. Thus, the red line does not indicate the theoretical  $P$  wave arrival, but the time at which enough energy hits the receiver to become observable. In a nonscattering environment, this would coincide with the theoretical  $P$  wave arrival time (Figure 8a). Increased levels of scattering can distribute wave energy over a long time, generating very emergent wave arrivals. This can impede precise wave arrival picks as seen in the traces for models C2, C3, D5, and D6, because the initial direct  $P$  wave energy can be too weak to be observed. The uncertainty in picks would be even greater in the presence of ambient and instrument noise. The effect is greater for impact events than for deep sources because rays from impacts tend to hit the base of the scattering layer at a shallower angle, and this energy thus travels a longer distance in the scattering layer before reaching the receivers.

The substantial visual differences among some of the traces are good initial indicators of the influence that the seismic velocities, scattering, and attenuation environment each have on surface recordings. Traces from models with lower scattering such as models D1, D2, and D3, overall have distinct  $P$  and  $S$  wave codas. Traces from models with higher levels of scattering such as C3 and D6 have traces that show a blended  $P$  and  $S$  wave coda. Another important difference among the traces is the apparent signal length. The total signal length of scattered signals is dependent on the initial energy released at the source and on how fast this energy decays near the receivers. For all events we released the same number of phonons (i.e., same total

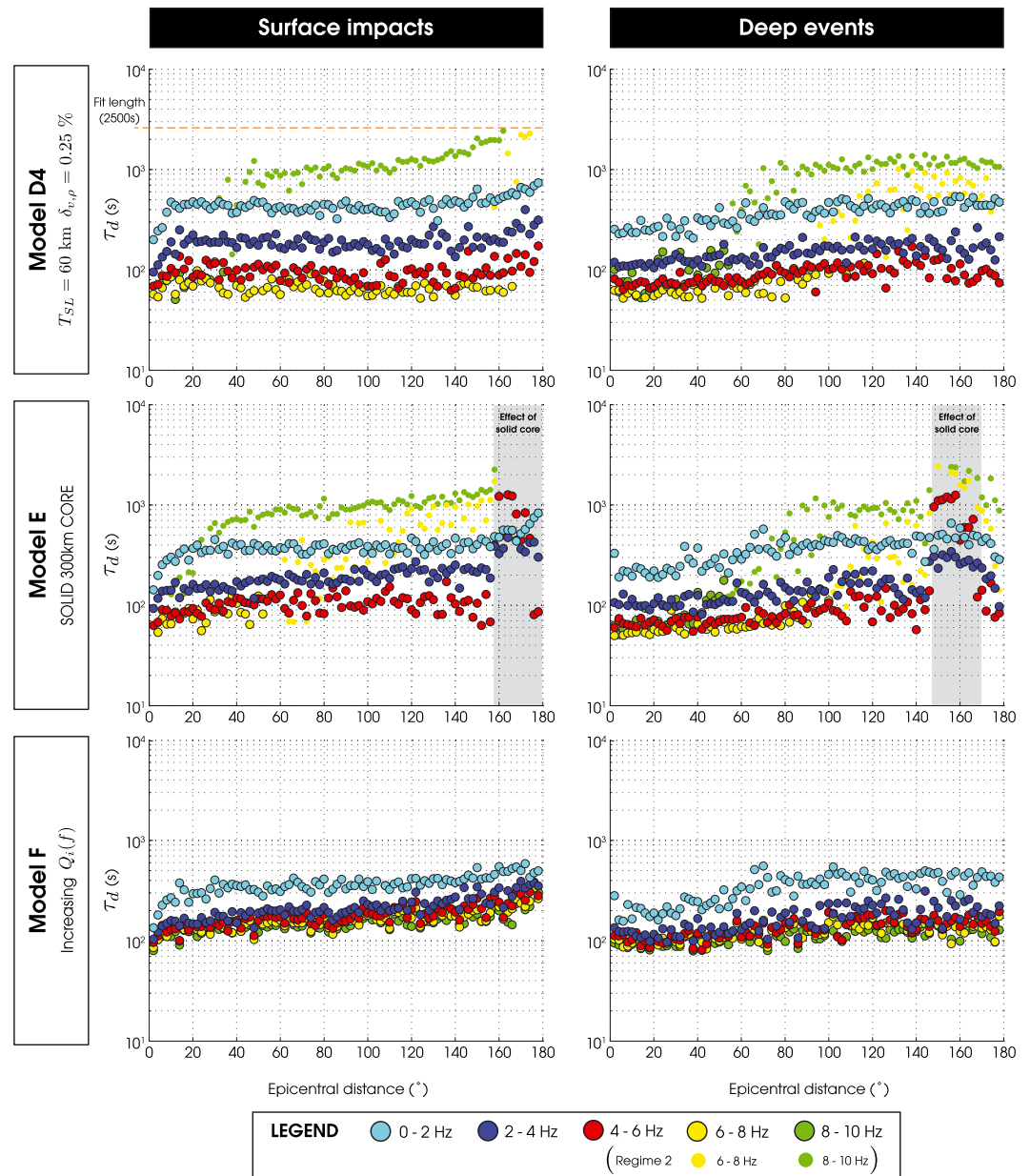


**Figure 12.** Decay times as a function of epicentral distance for 3 of the 16 investigated models. (left column) Decay times,  $\tau_d$ , for a surface impact; (right column) decay times for a 1000 km deep source. The different colors represent the different frequency bands. The least squares fit length of 2500 s is shown in the top left plot. All decay times larger than 2500 s were discarded. The transition from regimes 1 to 2 can be seen in the 6–8 Hz and 8–10 Hz bands in models D4 and F. On the other hand, the intrinsic attenuation levels in model F were low enough that all codas remain in Regime 1.

energy at the source), but some recordings, especially those from models with high scattering levels, show a much longer duration signal.

We present an example of detailed results from the coda decay fits in Figure 12 for models D4, E, and F. We show  $\tau_d$  as a function of epicentral distance, for the five investigated frequency bands, for both impacts (Figure 12, left column) and deep events (Figure 12, right column). All impact events exhibit a sharp rise in  $\tau_d$  values at short epicentral distances, tend to stabilize at larger distances, and may display another short rise at very large distances. Deep events show similar behavior but without the sharp rise  $\tau_d$  values at short epicentral distances. The effect of  $Q_i(f)$  on the coda decays can be addressed by observing  $\tau_d$  in different frequency bands.  $\tau_d$  clearly decreases with increasing frequency for models with a constant  $Q_i(f)$  (e.g.,

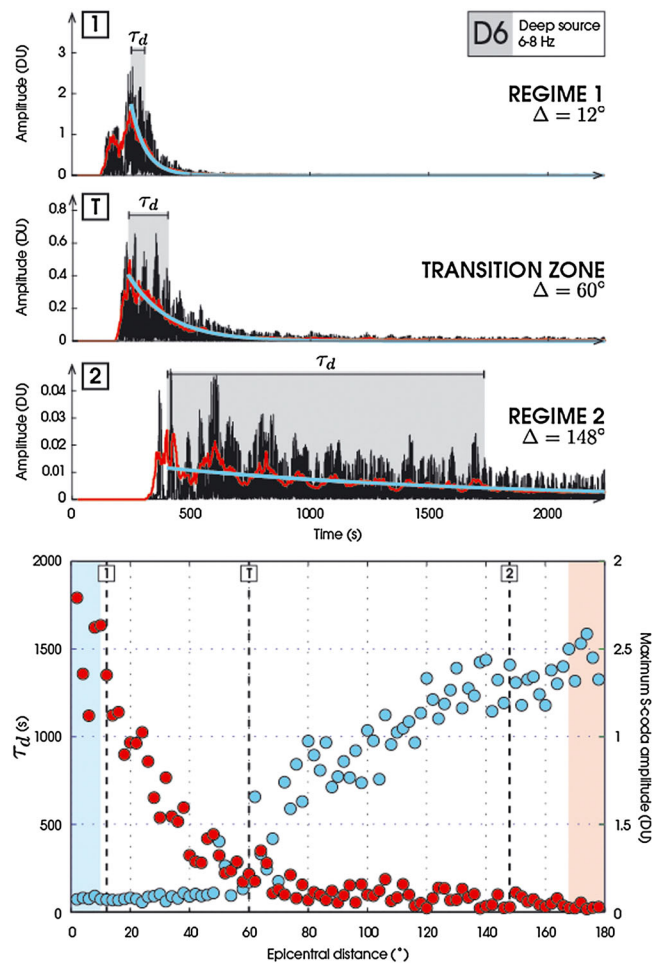


**Figure 13.** Traces and decay times for a deep source event in model D6, showing the transition between Regimes 1 and 2. Only traces and results from the 6–8 Hz frequency band are shown. (first to third rows) The envelope functions (black), the smoothed envelope functions (red), and the least squares fits (blue) for traces at epicentral distances  $\Delta = 12^\circ$ ,  $60^\circ$  and  $148^\circ$ . (fourth row) The change in  $\tau_d$  (blue) and maximum S coda amplitude (red) values as a function of epicentral distance.

frequency band. High-frequency bands transition to Regime 2 at smaller epicentral distances than lower frequencies. In fact, in most of the models under investigation, scattered codas in the 8–10 Hz band are in Regime 2, at least at larger epicentral distances. On the other hand, scattered codas in the 0–2 Hz band always remain in Regime 1. This frequency-dependent transition is demonstrated in Figure 12 (top, right) (model D4, deep events). The transition occurs first in the 8–10 Hz band, starting at around  $40^\circ$  and ending around  $80^\circ$ , and is followed by the 6–8 Hz band with a transition between  $90^\circ$  and  $140^\circ$ .

Figure 13 presents synthetic traces and decay fits for traces in Regime 1, in the transition zone, and in Regime 2. We also show the change in  $\tau_d$  and maximum S coda amplitude values as a function of epicentral distance. The synthetic traces,  $\tau_d$ , and amplitude values were measured in the 6–8 Hz band of a model D6 deep event. It is evident that Regime 1 is characterized by much larger amplitudes than Regime 2. The transition between the two regimes occurs when the change in maximum S coda amplitude as a function of epicentral becomes very small; i.e., the maximum S coda amplitude reaches a near-constant low value for the remaining epicentral distances.

The differences between decays in Regimes 1 and 2 are clearly expressed in Figure 14 which shows histograms of the averaged  $\tau_d$ , maximum S coda amplitudes and  $Q_c$  values for impacts and deep events. The average  $\tau_d$  values are calculated over the distance range in which the  $\tau_d$  values are approximately

models D4 and E in Figure 12). On the other hand, models with an increasing  $Q_i(f)$  (e.g., model F), shows a clustering of  $\tau_d$  values at high frequencies.

Two decay regimes have been identified. Regime 1 (larger outlined circles in Figure 12) is characterized by overall shorter decay times, whereas Regime 2 (smaller circles) has much longer decay times. These two regimes were identified in all models, and so we first discuss them in more detail below. We shall see that in practice Regime 1 is likely to be the regime that is relevant to seismograms recorded on a planetary surface, and so we then proceed to discuss the results for coda decay times for Regime 1 from the suite of interior structure models studied here. We note that the level of scattering in model D1, with a 5 km scattering layer ( $T_{SL} = 5$  km) and lower maximum velocities and density perturbation levels, was too low to generate codas adequate for fitting, and so no further results are shown from that model.

### 5.1. Two Distinct Decay Regimes

Figure 12 shows that the transition between Regimes 1 (shorter decay times) and 2 (longer decay times) is gradual and occurs over a fairly large range of epicentral distances. This range varies depending on the internal structure model and on the

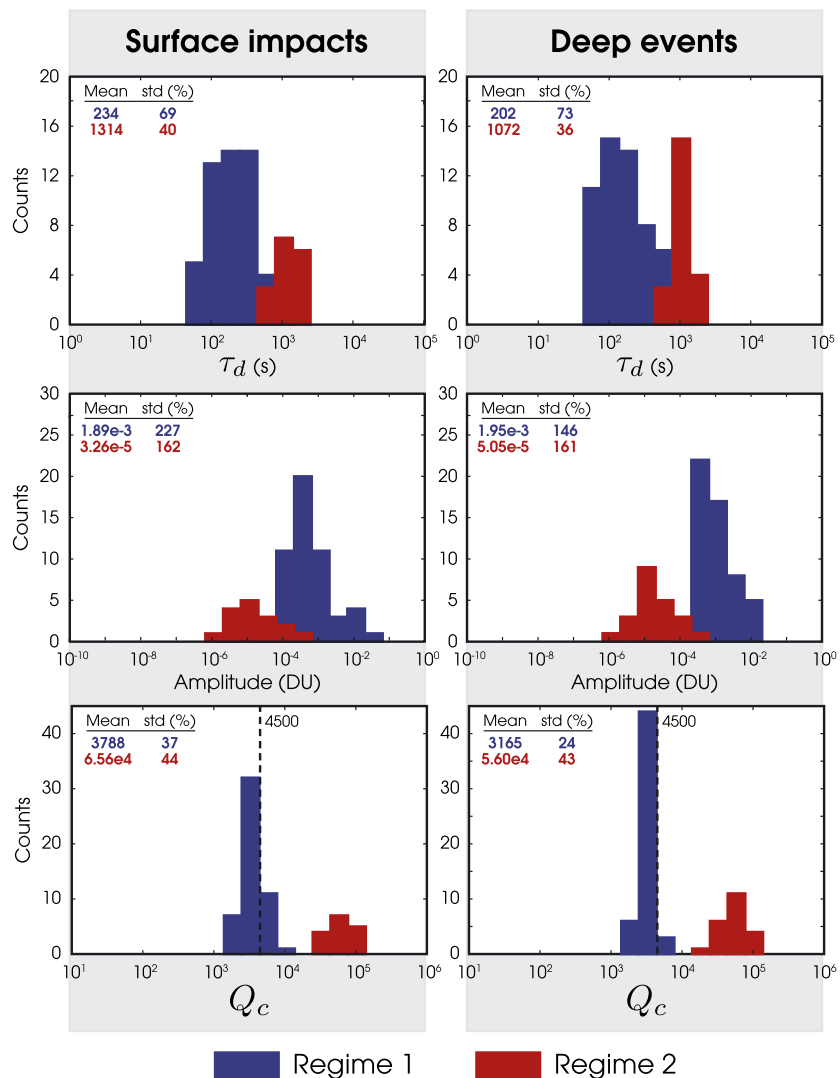


**Figure 14.** Histograms showing the (top rows) average  $\tau_d$ , (middle rows) maximum S coda amplitudes, and (bottom rows)  $Q_c$  values for Regimes 1 (blue) and 2 (red), and for (left column) impact events and (right column) deep events. The mean values for each regime are indicated, along with the standard deviation given as a percentage of the mean. Only models for which  $Q_i(f) = 4500$  are compiled here. Results from all frequency bands are included. The dashed lines in the  $Q_c$  plots show the  $Q_i$  value used.  $Q_c$  results to the left of that line indicate that the codas decay faster than they would if intrinsic attenuation was the only process by which energy was reduced.

constant for either Regime 1 or Regime 2. Results from all frequency bands are included, from all models with a constant  $Q_i(f) = 4500$ . There is a distinct difference in the mean decay time and mean S coda amplitude values between the two regimes. Models with lower intrinsic attenuation levels will have less energy transitioning to Regime 2. For example, codas from model F, which have an increasing  $Q_i$  (lower attenuation) for increasing frequency, have no decay in Regime 2 (Figure 12).

The maximum amplitude coda in Regime 2 is close to the average signal's coda amplitude, and typically, there are only two characteristic decay times in the 2500 s long fits, as compared with 10 or more in Regime 1. As such, the decay times for Regime 2 decays are less well estimated, and, in fact, Regime 2 may not be best estimated by an exponential decay. Further modeling work with longer traces would be necessary to investigate this, which is beyond the scope of the work presented here. However, it is still valid to state that at some distance exponentially decaying scattered signals (Regime 1) become so scattered that the recorded ground deformations are similar to very slowly decaying and very low amplitude seismic noise (Regime 2). This occurs at high frequencies first, because of the larger number of small-scale scatterers than large-scale ones, and because high frequencies go through more cycles over same time period than

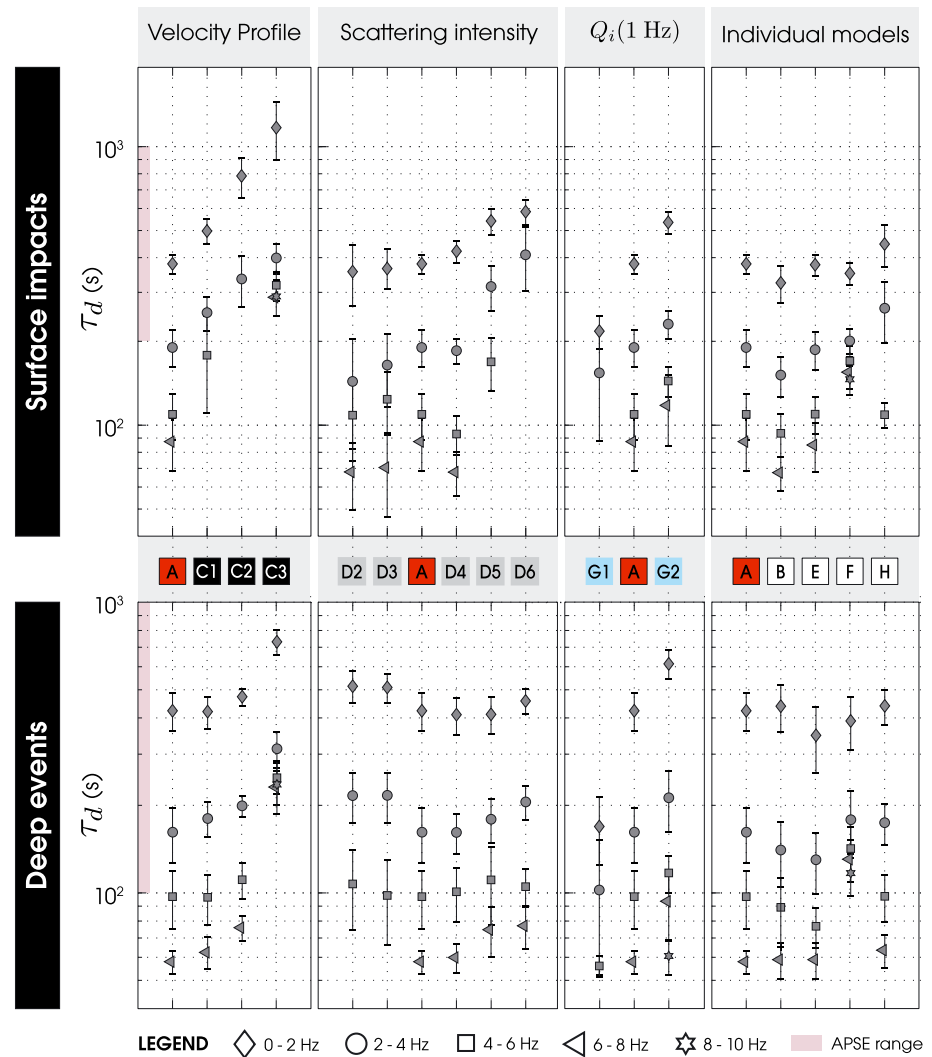


**Figure 15.** Plots showing the average  $\tau_d$  values for each models and each frequency bands, for (top row) surface impacts and (bottom row) deep events. Each symbol stand for a different frequency band and the error bars represent one standard deviation about the mean. Only the  $\tau_d$  from Regime 1 are shown. In some model,  $\tau_d$  were in Regime 2 for the entire range of epicentral distances and are thus not included here. The pink bars show the range of  $\tau_d$  present in the Apollo Passive Seismic Experiment (APSE) data set as comparison [Blanchette-Guertin *et al.*, 2012]. Models have been grouped based on which model parameters they help investigate, and each are plotted against the baseline model A. Models C1, C2, and C3 help identify the effect of the velocity profiles that increasingly trap seismic energy near the surface. The scattering intensity (combining both  $T_{SL}$  and  $\delta_{v,\rho}$ ) is investigated with models D2 to D6. The effect of a lower and larger  $Q_i(1 \text{ Hz})$  is shown with models G1 and G2. Model B shows the effect of halving the scattering layer thickness and the scatterer length scales (i.e., as many interaction with scatterers as in model A). Model E demonstrates the lack of effect that a small solid core has on the average  $\tau_d$  values. Model F has increasing  $Q_i$  values for increasing frequencies ( $Q_i$  style 2 compared to style 1 in model A). Model H shows the effect of a low scattering level in the interior.

low frequencies and are thus more attenuated. Regime 2 decays thus occur when most of the *P* and *S* wave impulsive signals have been reduced to very low amplitudes and very long duration source functions through intrinsic attenuation and scattering.

In Figure 14 we also compare the measured  $Q_c$  values with  $Q_i$  ( $= 4500$  for the models shown).  $Q_c$  values for Regime 1 decays are on average slightly less than  $Q_i$ . We propose that in high scattering environments, energy reaching the receiver is partially trapped locally. This is mainly due to the scattering layer reflecting the energy back toward the receiver, effectively mimicking a nearly closed system. In this case, intrinsic attenuation is the main process by which energy levels are reduced. The fact that individual  $Q_c$  values are slightly less or more than  $Q_i$  implies that some leakage or focusing of energy occurs, due to the particular

interior structure of each model. Still, we conclude that  $Q_c$  values of Regime 1 decays are good first-order indicators of intrinsic attenuation levels (i.e., good first-order approximation of the local  $Q_i$ ).  $Q_c$  values from Regime 2, on the other hand, are all larger than the models  $Q_i(f)$ , suggesting high-frequency energy is focused near the surface. However, the low amplitudes and less well-constrained least squares fits prohibits any further interpretations of Regime 2.

In the following sections, all interpretation regarding the effects of the velocity profile, and attenuation and scattering structure on the coda decays uses the Regime 1 decays. This is the regime likely to be measured with surface instruments given the much larger amplitudes.

## 5.2. Effects of Interior Structure on Coda Decay Times

Given the large amount of data, we characterize the  $\tau_d$  as a function of epicentral distance and frequency using an average Regime 1  $\tau_d$  calculated over the distance range in which the  $\tau_d$  values are approximately constant. We summarize these average  $\tau_d$  values for all models and frequency bands in Figure 15. Models A, C1, C2, and C3 show the effect of 1-D velocity profiles that increasingly tend to trap seismic energy in lower velocity layers near the surface and in the scattering layer. Models A and D2 to D6 illustrate the changes in coda decay for increasing levels of scattering (implemented using increasingly thicker scattering layers and by varying the maximum velocity and density perturbation levels). Models A, G1, and G3 emphasize the effect of reducing or increasing the reference intrinsic attenuation factor  $Q_i(1 \text{ Hz})$ . Model B halves the scattering layer thickness ( $T_{SL} = 15 \text{ km}$ ) and the minimum and maximum scatterer length scales, such that the seismic energy interacts with the same amount of scatterers, but in a thinner scattering layer. Model E shows the effects of having a small solid core on the averaged  $\tau_d$ . Model F illustrates the effect of a constant versus an increasing  $Q_i$  with frequency (i.e., lower intrinsic attenuation at high frequency). Finally, model H is used to show the effect of low-level global scattering on the coda.

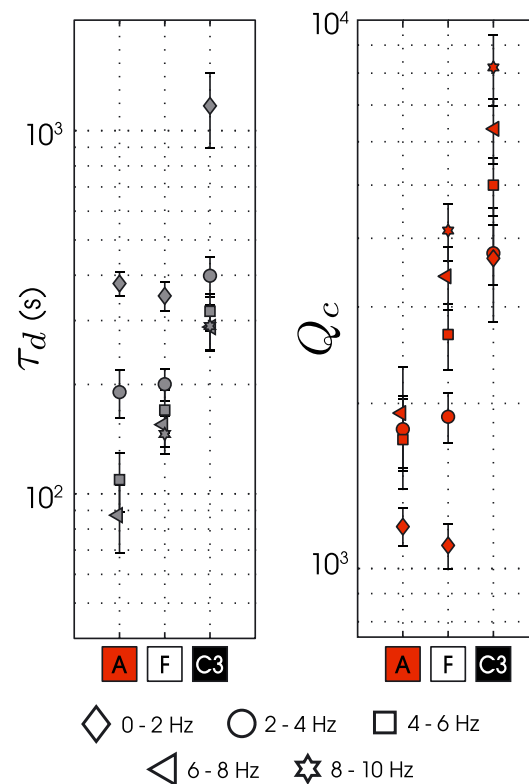
### 5.2.1. Sharp Rise in Impacts $\tau_d$ Rimes at Short Distances

Figure 12 shows an increase in  $\tau_d$  values for impact events between  $0^\circ$  and approximately  $10^\circ$ . This increase is seen in all models, including those not presented in Figure 12. Furthermore, a similar trend is observed in the APSE seismic lunar data [see *Blanchette-Guertin et al.*, 2012, Figure 5]. The rate of increase, as well as the exact distance at which  $\tau_d$  becomes near constant appear to be model dependent, suggesting that these parameters could be used to infer first-order near-surface interior structure properties such as the thickness of the scattering layer and scattering intensity. However, the receiver sampling distance used in our modeling ( $2^\circ$ ) is too large to assess precisely differences among models. Further modeling could investigate this near-source effect, its potential as a geophysical tool and any specific application to the Apollo seismic data.

We propose that the distance at which the sharp rise in decay times ends relates to the distance at which the seismic energy traveling between the source and the receivers stops interacting only with the scattering layer and starts to have a substantial fraction of the travel path in the underlying nonscattering (or less highly scattering) lower crust or mantle. Our model impact source function is an impulsive delta function ( $\tau_d \rightarrow 0$ ). This initial impulse spreads out as it travels in the scattering layer. Each adjacent receiver is hit by an increasingly diffused source function that traveled primarily within the scattering layer, with closer receivers seeing a more impulsive arrival (shorter  $\tau_d$ ) than the more distant ones (longer  $\tau_d$ ). Distant receivers ( $>10^\circ$ ) all see a similar source wave function that has left the scattering layer near the source and traveled in the mantle to reenter the scattering layer at all point near the receivers.

### 5.2.2. Velocity Profile

The velocity profile is one of the parameters that has the biggest impact on the characteristics of the scattered codas, especially for impact events. Models A, C1, C2, and C3 have velocity profiles that increasingly tend to trap or focus seismic energy near the surface and in the scattering layer. This results in increasingly large decay times, for example, from  $\tau_d(1 \text{ Hz}) = 380 \text{ s}$  in model A to  $\tau_d(1 \text{ Hz}) = 1170 \text{ s}$  in Model C3 for impact events. Benchmark model A has only mantle velocities and scattering in the scattering layer is the only process by which the energy remains near the surface. Model C1 introduces a crust/mantle boundary, which will reflect some downgoing rays up into the scattering layer. Model C2 not only has a crust but also has a near-surface, thin, very low velocity layer analogous to a regolith layer. This layer is particularly effective in trapping energy from impact events near the surface and in the scattering layer. Model C3 has a crust, a thin low velocity layer, and a more realistic velocity gradient (velocities increase with



**Figure 16.** (left)  $\tau_d$  and (right)  $Q_c$  for impact events from models A, F, and C3. Model A has a constant  $Q_i(f)$  (style 1 in Figure 10). Models F and C3 have an increasing  $Q_i(f)$  with increasing frequencies (style 2 in Figure 10). Changes in  $\tau_d$  and  $Q_c$  as a function of frequency is dependent on  $Q_i(f)$ . For model A,  $\tau_d$  values decrease as a function of frequency, whereas for models F and C3,  $\tau_d$  values tend to cluster around a constant value (except for the 0–2 Hz band). The opposite is true for  $Q_c(f)$ . Model A values, except for the 0–2 Hz band, cluster around 1800, whereas  $Q_c$  values increase with increasing frequency for models F and C3. As such, comparing  $\tau_d(f)$  and  $Q_c(f)$  can be useful to assess the properties of  $Q_i(f)$ .

scatterer length scale distribution. None of these models had a velocity profile that was conducive to trapping the energy near the surface and we infer that this is why changing the scattering layer structure has a bigger effect for impact events than for deep events.  $\tau_d(f)$  values for deep events tend to be within one standard deviation of the mean values of all other models and do not seem much affected by variations in  $T_{SL}$  and  $\delta_{v,\rho}$ . In fact, most of the deep event energy will hit the scattering layer at a fairly steep angle and spend less time overall in the layer than energy from impact events.

For impact events both the scattering layer thickness and the average impedance contrast affect the level of scattering and the resulting decay times. Models D3, A, and D5 all have  $\delta_{v,\rho}$  set at 75% but have successively increasing scattering layer thicknesses. It follows that  $\tau_d$  values from model D5 ( $T_{SL} = 60$  km) are larger than those from model A ( $T_{SL} = 30$  km) and from model D3 ( $T_{SL} = 5$  km), with  $\tau_d$  of 541, 380, and 370 s in the 0–2 Hz band, respectively. The same is true of increasing impedance values:  $\tau_d$  values increase from models D4 to D6 which all have a similar scattering layer thickness (421 s, 541 s, and 583 s in the 0–2 Hz band). Note that  $\tau_d$  values for the 4 to 10 Hz frequency bands are not shown for model D6, as the high levels of scattering caused these bands to be in Regime 2 at all epicentral distances.

Both increasing impedance contrasts at the scatterers and an increasing scattering layer thickness will result in longer coda decay times. However, a high impedance contrast does not necessarily generate long

depth) which causes the rays to turn at depth, sending them back near the surface sooner than in models without a gradient.

Thus velocity profiles that are conducive to focusing seismic energy near the surface and/or in the scattering layer can drastically increase the coda decay times. We found that for all other attenuation and scattering parameters remaining equal, the velocity profile has the biggest impact on the decay times.

### 5.2.3. Scattering Layer Thickness and Impedance Contrast

Models A and D2 to D6 show the effect of increasing the scattering layer thickness and the impedance contrast on the coda decays. The impedance contrast is incorporated in our model as the maximum variations from the background density and velocities at each scatterers ( $\delta_{v,\rho}$ ). A small  $\delta_{v,\rho}$  means that most phonons will hit scatterers with low-velocity and density contrast and that most will be transmitted with only small variations to their original path and so weak forward scattering is preferred. On the other hand, a large  $\delta_{v,\rho}$  will cause more phonons to be widely scattered off path resulting in more isotropic scattering. Low impedance contrasts (e.g.,  $\delta_{v,\rho} = 25\%$ ) may be analogous to interaction with annealed fractures or interfaces between two similar lithologies, whereas large impedance contrasts (e.g.,  $\delta_{v,\rho} = 95\%$ ) may be analogous to high porosity levels. Models D2 and D3 have a 5 km thick scattering layer, with  $\delta_{v,\rho}$  values of 75 and 95%, respectively. Models D4, D5, and D6 all have a much thicker scattering layer ( $T_{SL} = 60$  km) and  $\delta_{v,\rho}$  equal to 25, 75, and 95%. These are compared to the baseline model A that has  $T_{SL} = 30$  km,  $\delta_{v,\rho} = 75\%$ . All models used the same

scattered coda if the scattering layer is insufficiently thick because there will not be enough interactions with scatterers. An example is model D3, which has  $T_{SL} = 5$  km with a maximum impedance contrast of 95%.

#### 5.2.4. Intrinsic Attenuation

Models G1, A, and G2 show the effect of various levels of intrinsic attenuation with  $Q_i(1\text{Hz}) = 2500, 4500,$  and  $6000$ , respectively. This corresponds to decreasing levels of intrinsic attenuation. In all models,  $Q_i(f)$  is constant, resulting in high frequencies that attenuate faster than lower frequencies, because they go through more cycles for similar time periods. Results show that decay times increase for increasing  $Q_i(1\text{ Hz})$ , at all frequency levels. Decay times in the 0–2 Hz band for impact events increase from 154 s in model G1, to 380 s in model A, and up to 535 s in model G2. In addition, the higher-attenuation level of model G1 causes more frequency bands to switch to Regime 2 scattering and only the 0–2 and 2–4 Hz bands have codas in the Regime 1. The effect is similar for deep events. Overall, our results show that an increase in  $Q_i$  by a factor of 2 or 3 can yield similar increase in  $\tau_d$ , depending on the frequency.

The behavior of  $\tau_d(f)$  and  $Q_c(f)$  can be used to assess the properties of  $Q_i(f)$ , as can be seen with the results from models A, C3, and F. Model A has a constant  $Q_i(f)$ , whereas models C3 and F have an increasing  $Q_i(f)$ , with  $Q_i = 4500$  in the 0–2 Hz band as in model A, 7200 in the 2–4 Hz band, 9900 in the 4–6 Hz band, 12600 Hz in the 6–8 Hz band, and 15,300 in the 8–10 Hz band. The attenuation differences are reflected in the decay times and factors. The  $\tau_d$  in model A decreases as a function of frequency (as seen in Figures 15 and 16), the corresponding  $Q_c$  values, however, tend to cluster, at least for frequencies above 2 Hz. The opposite is true for models C3 and F, where the  $\tau_d$  values cluster in the 2–10 Hz band, and where  $Q_c(f)$  increases with frequency. This observation is particularly important as a similar behavior is seen in the Apollo lunar seismic data (clustering of  $Q_c$  values at low frequencies and clustering of  $\tau_d$  values at high frequencies, as shown in *Blanchette-Guertin et al.* [2012]). This suggests a near-constant  $Q_i(f)$  for lower lunar seismic frequencies (0.5–1.5 Hz) and an increasing  $Q_i$  with increasing frequency for the higher-frequency range (2–10 Hz).

#### 5.2.5. Scatterer Density and Scattering Time

Model B is similar to model A, except that the scattering layer thickness and the minimum and maximum scatterer length scales are halved. This means that phonons in both models interact with the same amount of scatterers. In other words, the *scatterer density* in model B is twice that of model A, but the scattering layer thickness in B is half that of model A. One would expect similar decay times for both models, given that they interact with as many scatterers. However,  $\tau_d$  values from model B are overall less than  $\tau_d$  from model A. This may be due fact that although the seismic energy in model B interacts with as many scatterers as the energy in model A, the path length between those scatterers will be half as long, such that scattered energy will be delayed less relatively to the geometric path than in model A. This leads to overall shorter decay times. One might expect a more drastic drop in decay times in model B (close to half of that of model A), but because the energy in model B spends less time in the scattering layer, it will also be less attenuated, and this effect acts to increase the decay times.

#### 5.2.6. Presence of a Solid Core

The presence of a small solid core (model E) has little effect on the average decay times for either surface impact or deep events (as seen in Figure 15). We observe a slight decrease in  $\tau_d$  for the deep events when compared to model A values, but all  $\tau_d$  remain within one standard deviation of each other. This lack of effect on the average  $\tau_d$  is mostly due to the fact that most of the direct *P* and *S* wave energy leaving the sources does not actually interact with the core. The effect of the core does show up, however, at larger distances, where no direct *P* or *S* wave energy hits the surface (the core shadow zone, see Figure 12 (middle row) showing increased  $\tau_d$  in shadow zone). Decay times in this region are much larger. Our results also indicate that maximum *S* coda amplitudes at stations within the shadow zone are smaller by about 2 orders of magnitude than coda amplitudes at stations just adjacent to the shadow zone. We propose that in high scattering environments, the energy that makes it to surface recorders in the core shadow zone has leaked from the surrounding scattering layers. This scattered leaked energy dominates the signal, in contrast to the other stations where energy from the direct *P* and *S* wave arrivals dominate.

#### 5.2.7. Low-Level Mantle Scattering

Model H introduces low-level scattering in the planetary body's interior. The scatterer length scale outside of the scattering layer was set to 10 km, with a scattering probability of 0.01. This means that a phonon interacts with a scatterer approximately every 1000 km of travel distance in the interior.  $\delta_{v,p}$  was set to 75%, similar to that in the scattering layer. Low-level mantle scattering slightly increases the average  $\tau_d$  for both impact and deep events, as observed by comparing models A and H values in Figure 15. This increase in

average  $\tau_d$  is caused by a slowly increasing  $\tau_d$  with increasing  $\Delta$  (not shown here). This is in turn due to the fact that traveling phonons hitting the base of the scattering layer at large distances will have been scattered more in the interior than those hitting the scattering layer near closer receivers. Another effect of interior scattering can be observed by comparing traces from models A and H in Figure 11. For the impact events, low-level mantle scattering will effectively blend the *P* and *S* wave codas, effectively obscuring the *S* wave arrival (bottom left trace). Low-level mantle scattering as implemented in this model appears to have a negligible effect on deep event traces, except for lengthening the decay time and slightly accentuating the *P* wave coda.

## 6. Conclusions

We used a phonon method to model the propagation of seismic energy in highly scattering environments. We have generated synthetic traces and measured their characteristic decay times and decay factors to assess the effects of various velocity, attenuation, and scattering parameters on the seismic signals. The main observations and conclusions of this study are

1. High levels of seismic energy scattering will generate ground deformation with amplitudes that decay exponentially (Regime 1), until intrinsic attenuation and scattering transform the traveling source function and the resulting ground deformation into very low amplitude, slowly decaying noise-like signals (Regime 2). Our modeling work favored higher scattering levels and faster attenuation for high frequencies and as such, high frequencies transition to Regime 2 at shorter epicentral distances than lower frequencies.
2. We observed a sharp rise in characteristic decay times at short epicentral distances ( $0^\circ$  to  $\sim 10^\circ$ ) for impact events, after which  $\tau_d$  values stabilize. The distance at which  $\tau_d(\Delta)$  stabilizes and the rate of increase at lower values of  $\Delta$  appear to be model dependent, suggesting these values, together with further modeling, could be used to infer first-order near-surface interior structure properties such as the thickness of the scattering layer and the scattering intensity.
3. Velocity structures that tend to trap and focus seismic energy near the surface and in the scattering layer have considerable effect on the characteristic decay times. A crust-mantle boundary, the presence of a thin very low velocity layer near the surface (e.g., the lunar regolith), or a sharp velocity gradient with depth increased the decay times by up to at least a factor of 4 in the models investigated here. This effect is also larger for shallow events—impacts or quakes—than for deep events.
4. Both the impedance contrast at the scattering interfaces and the scattering layer thickness have an effect on the resulting seismic codas. Larger impedance contrasts and a thicker scattering layer will lead to longer decay times. However, a thick scattering layer with lower levels of impedance can scatter energy more than a thin scattering layer with high levels of impedance, at least in the manner in which impedance was modeled in our study.
5. Our modeling showed that higher-attenuation levels (lower  $Q_i$ ) will lead to shorter decay times and conversely that lower attenuation levels result in longer decay times. An increase in  $Q_i$  by a factor of 2 or 3 can yield similar increase in  $\tau_d$ , depending on the frequency band.  $Q_c$  values of Regime 1 signals are good first-order indicators of the near-station intrinsic attenuation level,  $Q_i$ . Similarly, the change of  $Q_c$  as a function of frequency can be used to assess  $Q_i(f)$ : Near-constant  $Q_c(f)$  suggests a constant  $Q_i(f)$ , whereas  $Q_c$  values that are increasing with frequency indicate an increasing  $Q_i$  with frequency.
6. Deep structures such as a small core have little impact on the decay times. Any effect seems to be spatially limited to the core's direct *P* and *S* wave shadow zone. Energy is observed in the shadow zone even if no direct wave can propagate into the region, as the energy leaks from the surrounding scattering layer. At these epicentral distances, the maximum *S* coda amplitudes are much lower, and the decay times much longer.
7. Increasing  $\tau_d$  as a function of epicentral distance suggests low levels of seismic scattering in the interior. Interior scattering also tends to blend the *P* and *S* wave codas, making it harder to identify with precision the location of the *S* wave arrival.

The velocity profile, intrinsic attenuation, and scattering structures of highly scattering planetary bodies have a considerable effect on the duration and form of the resulting ground deformations. Our ability to model and understand these effects will lead to better interpretations of current and future seismic data sets and will provide us with a clearer understanding of the interiors of planetary objects under investigation.

### Acknowledgments

We acknowledge support from the Natural Sciences and Engineering Research Council of Canada (J.-F.B.G. and C.L.J.) and from NASA grant NNX11AB55G (J.F.L.). We thank Mark Panning for his insightful review of the manuscript as well as two anonymous reviewers for helpful comments. All modeling data can be obtained by contacting the corresponding author.

### References

- Aki, K. (1969), Analysis of the seismic coda of local earthquakes as scattered waves, *J. Geophys. Res.*, *74*(2), 615–631.
- Aki, K., and B. Chouet (1975), Origin of coda waves: Source, attenuation, and scattering effects, *J. Geophys. Res.*, *80*(23), 3322–3342.
- Aki, K., and P. G. Richards (2009), *Quantitative Seismology*, 2nd ed., 700 pp., Univ. Sci. Books, Sausalito, Calif.
- Ben-Menahem, A., and S. J. Singh (1981), *Seismic Waves and Sources*, Springer, Berlin.
- Bhattacharya, S. (1972), Exact solutions of the equation for the free torsional oscillations of an inhomogeneous sphere, *Bull. Seismol. Soc. Am.*, *62*, 31–38.
- Bhattacharya, S. (1996), Earth flattening transformation for P-SV waves, *Bull. Seismol. Soc. Am.*, *86*, 1979–1982.
- Bhattacharya, S. (2005), Synthetic seismograms in a spherical Earth using exact flattening transformation, *Geophys. Res. Lett.*, *32*, L21303, doi:10.1029/2005GL024152.
- Blanchette-Guertin, J.-F., C. L. Johnson, and J. F. Lawrence (2012), Investigation of scattering in lunar seismic coda, *J. Geophys. Res.*, *117*, E06003, doi:10.1029/2011JE004042.
- Boatwright, J., and J. Fletcher (1984), The partition of radiated energy between P and S waves, *Bull. Seismol. Soc. Am.*, *74*(2), 361–376.
- Dahlen, F. (2005), Finite-frequency sensitivity kernels for boundary topography perturbations, *Geophys. J. Int.*, *162*(2), 525–540.
- Fuchs, K. (1968), The reflection of spherical waves from transition zones with arbitrary depth-dependent elastic moduli and density, *J. Phys. Earth*, *16*, 27–41.
- Fuchs, K., and G. Müller (1971), Computation of synthetic seismograms with the reflectivity method and comparison with observations, *Geophys. J. R. Astron. Soc.*, *23*(4), 417–433.
- Garcia, R. F., J. Gagnepain-Beyneix, S. Chevrot, and P. Lognonné (2011), Very preliminary reference Moon model, *Phys. Earth Planet. Inter.*, *188*, 96–113, doi:10.1016/j.pepi.2011.06.015.
- Gusev, A., and I. Abubakirov (1987), Monte-Carlo simulation of record envelope of a near earthquake, *Phys. Earth Planet. Inter.*, *49*, 30–36.
- Hörz, F. (1991), Lunar surface processes, in *The Lunar Sourcebook*, edited by G. H. Heiken et al., pp. 62–120, Pergamon, New York.
- Hoshiba, M. (1994), Simulation of coda wave envelope in depth dependent scattering and absorption structure, *Geophys. Res. Lett.*, *21*(25), 2853–2856.
- Jin, A., and K. Aki (1986), Temporal change in coda Q before the Tangshan earthquake of 1976 and the Haicheng earthquake of 1975, *J. Geophys. Res.*, *91*, 665–673, doi:10.1029/JB094iB10p00665.
- Knapmeyer, M. (2004), TTBBox: A MATLAB toolbox for the computation of 1D teleseismic travel times, *Seismol. Res. Lett.*, *75*(6), 726–733.
- Latham, G. V., M. Ewing, F. Press, G. Sutton, J. Dorman, Y. Nakamura, N. Toksoz, R. Wiggins, and R. Kovach (1970a), Passive seismic experiment, in *Apollo 12 Preliminary Science Rep. NASA SP-235*, pp. 39–54, NASA, Washington, D. C.
- Latham, G. V., et al. (1970b), Passive seismic experiment, *Science*, *167*(3918), 455–457.
- Margerin, L., M. Campillo, and B. van Tiggelen (1998), Radiative transfer and diffusion of waves in a layered medium: New insight into coda Q, *Geophys. J. Int.*, *134*, 596–612.
- Margerin, L., M. Campillo, and B. V. Tiggelen (2000), Monte Carlo simulation of multiple scattering of elastic waves, *J. Geophys. Res.*, *105*(B4), 7873–7892.
- Mayeda, K., S. Koyanagi, M. Hoshiba, K. Aki, and Y. Zeng (1992), A comparative study of scattering, intrinsic, and coda  $Q^{-1}$  for Hawaii, Long Valley and Central California between 1.5 and 15 Hz, *J. Geophys. Res.*, *97*, 6643–6659, doi:10.1029/91JB03094.
- Nakamura, Y. (1977), Seismic energy transmission in an intensively scattering environment, *J. Geophys.*, *43*, 389–399.
- Nakamura, Y., F. K. Duennebieber, G. V. Latham, and H. J. Dorman (1976), Structure of the lunar mantle, *J. Geophys. Res.*, *81*(26), 4818–4824.
- O'Keefe, J., and T. Ahrens (1987), The size distributions of fragments ejected at a given velocity from impact craters, *Int. J. Impact Eng.*, *5*(1), 493–499.
- Przybilla, J., U. Wegler, and M. Korn (2009), Estimation of crustal scattering parameters with elastic radiative transfer theory, *Geophys. J. Int.*, *178*(2), 1105–1111, doi:10.1111/j.1365-246X.2009.04204.x.
- Sato, H. (1978), Mean free path of the S-waves under the Kanto district of Japan, *J. Phys. Earth*, *25*, 163–176.
- Sato, H., M. C. Fehler, and T. Maeda (2012), *Seismic Wave Propagation and Scattering in the Heterogeneous Earth*, 2nd ed., p. 484, Springer, Berlin.
- Shearer, P. M., and P. S. Earle (2004), The global short-period wavefield modelled with a Monte Carlo seismic phonon method, *Geophys. J. Int.*, *158*(3), 1103–1117, doi:10.1111/j.1365-246X.2004.02378.x.
- Weber, R., P.-Y. Lin, E. Garnero, Q. Williams, and P. Lognonné (2011), Seismic detection of the lunar core, *Science*, *331*(6015), 309–312.
- Wieczorek, M. A., et al. (2013), The crust of the Moon as seen by GRAIL, *Science*, *339*(6120), 671–675, doi:10.1126/science.1231530.
- Yoshimoto, K. (2000), Monte Carlo simulation of seismogram envelopes in scattering media, *J. Geophys. Res.*, *105*(B3), 6153–6161.
- Yoshimoto, K., and A. Jin (2008), Coda energy distribution and attenuation, *Adv. Geophys.*, *50*, 265–299, doi:10.1016/S0065-2687(08)00010-1.